255 (2025) 214060

Contents lists available at ScienceDirect

Geoenergy Science and Engineering

journal homepage: www.sciencedirect.com/journal/geoenergy-science-and-engineering

Simultaneous evolution of geochemical and petrophysical properties of lacustrine carbonaceous shales during thermal maturation

Juncheng Qiao [a,b,*], Jianhui Zeng [a,b,**], Guangqing Yang [c], Zhe Cao [c], Yazhou Liu [a,b], XiuJuan Zhang [a,b]

[a] State Key Laboratory of Petroleum Resources and Engineering, China University of Petroleum, Beijing, 102249, PR China
[b] College of Geosciences, China University of Petroleum, Beijing, 102249, PR China
[c] Sinopec Petroleum Exploration and Production Research Institute, Beijing, 102206, PR China

ARTICLE INFO

Keywords:
Lacustrine carbonaceous shale
Thermal maturation
Hydrous pyrolysis
Geochemical and petrophysical properties
Solid-fluid interactions

ABSTRACT

To explore the simultaneous evolution of the geochemical and petrophysical properties of carbonaceous shales during thermal maturation, hydrous pyrolysis experiments were performed on four lacustrine shales with different textures, collected from the Lucaogou formation of Jimsar sag in the Junggar Basin, China. To preserve the rock texture, pyrolysis was conducted on cm-sized prisms cut from drill cores. Samples were heated for 24 h to temperatures of 295, 320, 345, 370, and 400 °C. The original samples and the pyrolyzed residues were characterized by organic-geochemical (TOC, Ro, Rock-Eval, solvent extraction, compound group separation and analysis of the extracts and the liquid and gaseous products) and petrophysical characterization methods (low-pressure N_2 adsorption, X-ray CT). The onset of the decomposition of the organic matter (OM) at 295 °C and 320 °C (Ro 0.8 %–1.0 %) results in a more than eightfold increase of organic micro- and mesopores (1 - 100 nm), associated with the expulsion of light hydrocarbons from the matrix. At 325 °C, the TOC reduction rate was found to increase by 67 %–167 %, while fluid flow pathways were blocked by heavy bitumen with asphaltene content of ~20 %. This is associated with a weak increase or even decline in porosity and permeability at the end of low mature stage. The fast acceleration of OM decomposition at 345 °C gives rise to an excessive pressure due to fluid expansion, accompanied with a volume expansion of macropores (1 μm - 10 μm) and generation of microfractures >10 μm. Therefore, a secondary increase in porosity and permeability occurs, which promotes the expulsion of liquid hydrocarbons at 345°C - 370 °C. The rate of OM decomposition positively correlates with the expansion of the flow paths and the rate of expulsion of liquid product up to the end of mature stage. In the high mature stage (>370 °C), the laminated shale exhibits a continuous increase in porosity and permeability, while these parameters decline due to pore collapse and fracture healing in the massive shale. This decline appears to inhibit the transformation of OM, indicating that lamination is advantageous for OM transformation. Our results suggest that temperatures between 345 °C and 370 °C are favorable for in-situ retorting of laminated shales, while for the retorting of massive shales higher temperatures (~400 °C) are required. Rock fabric, lamination, maturation degree, and liquid residues should also be considered in the porosity and permeability evaluation and in-situ retorting program optimization of shale.

1. Introduction

The unconventional petroleum produced from fine-grained sediments has significantly impacts on the global energy structure (Curtis, 2002; Zou et al., 2013; Valenza et al., 2013; Zou et al., 2010, 2020; EIA, 2015). Carbonaceous shales deposited on ocean margins or in shallow inland waterways, are characterized by a complex rock fabric consisting of an inorganic mineral skeleton (IM) and organic matter (OM) (Hedges and Keil, 1995; Mayer et al., 2004; Curry et al., 2007; Potter et al., 2012; Zou et al., 2013; Crombez et al., 2017). Sedimentation, redistribution and bioturbation, produce a heterogeneous rock fabric, leading to varied geochemical and petrophysical properties of shales (Loucks et al., 2009; Wood and Hazra, 2017), which ultimately influence the shale oil and gas production (Dyni, 2003; Pollastro et al., 2008; Rickman et al., 2008;

* Corresponding author. State Key Laboratory of Petroleum Resources and Engineering, China University of Petroleum, Beijing, 102249, PR China.
** Corresponding author. State Key Laboratory of Petroleum Resources and Engineering, China University of Petroleum, Beijing, 102249, PR China.
E-mail addresses: Juncheng.Qiao@cup.edu.cn (J. Qiao), zengjh@cup.edu.cn (J. Zeng).

https://doi.org/10.1016/j.geoen.2025.214060
Received 7 February 2025; Received in revised form 31 May 2025; Accepted 21 June 2025
Available online 25 June 2025

Sondergeld et al., 2010; Glorioso and Rattia, 2012; Hao and Zou, 2013; Aguilera, 2014; Yang et al., 2017).

The petrophysical properties have been a long-term focus in basic studies of shales (Smith, 1971; Bennett, 1991; Ross and Bustin, 2009; Curtis, 2010, 2012b; Chalmers et al., 2012; Clarkson et al., 2013, 2016; Bahadur et al., 2014; Davudov and Moghanloo, 2018; Borjigin et al., 2021). The porosity, permeability, and nature, type, size distribution, connectivity, and configuration of the pore spaces controlling the storage and fluid flow capacities have been emphasized in the past decade (Clarkson et al., 2012; Curtis et al., 2012b; Yao and Liu, 2012; Cnudde and Boone, 2013; Sakhaee-Pour and Bryant, 2012; Sigal, 2015; Ma et al., 2017; Liu et al., 2018; Gou et al., 2019; Zhao et al., 2020; Arif et al., 2021; Xu et al., 2022). The effects of geochemical properties on the reservoir quality and pore structure have been discussed owing the presence of OM in the rock fabric (Bustin et al., 2008; Wang et al., 2009; Tiwari et al., 2013; Tang et al., 2016). The types (kerogen type), content (TOC), and maturity (R_O) of the OM exerts strong effects on the pore development and complexity (Jarvie et al., 2007; Bustin et al., 2008; Wang et al., 2009; Curtis et al., 2012a; Kuila et al., 2014), while recent studies reported that IM, such as clay and carbonate minerals, also has significant impacts on the pore structure of lacustrine shales (Kuila and Prasad, 2013; Löhr et al., 2015; Mishra et al., 2018; Han et al., 2020; Chang et al., 2022). Some evidence indicates that in some instances IM contributes three times more nanoporosity than OM. Moreover, organic-inorganic interactions, in particular catalytic or inhibiting effects of the IM on OM, also exert strong effects (Revil and Cathles III, 1999; Mastalerz et al., 2013; Milliken and Day-Stirrat, 2013; Mishra et al., 2018; Chang et al., 2022).

Thermal maturation outweighs other factors in affecting the microstructure of shale as it controls the thermochemical decomposition of kerogen, resulting in substantial modification of the pore network (Berner and Faber, 1996; Behar et al., 1997; Chen and Xiao, 2014; Wang et al., 2019, 2022; Song et al., 2020). This effect is of high relevance to the artificial maturation of shale, including overground retorting and subsurface in-situ pyrolysis industry. Thus, a deep understanding for the products, storage and migration pathways, and matrix skeleton during thermal maturation process that occurs over a wide range of length and time scales is required (Schrodt and Ocampo, 1984; Tiwari et al., 2013). Hydrous and anhydrous pyrolysis have been used in the investigation of the thermal evolution of shales, and the heating temperatures typically range from 200 to 600 °C, covering the main physical transformation of OM between 200 and 350 °C and chemical decomposition and thermal cracking between 350 and 600 °C (Tiwari et al., 2013; Xi et al., 2018a; 2018b; Li et al., 2020; Wang et al., 2020). The associated changes in pore structure are generally analyzed using low-temperature nitrogen absorption (LTNA), X-ray computed tomography (X-ray CT), nuclear magnetic resonance (NMR), and scanning electron microscopy (SEM) (Schrodt and Ocampo, 1984; Loucks et al., 2009; Tiwari et al., 2013; Liu et al., 2023a). Some of the investigations found an increase of micro-, meso-, and macro-porosity with maturity, however, opposite trends have been reported by Tang et al. (2016)and Xi et al. (2018a,b) in the high to overmature stage. Some more complicated phenomena has been observed, such as broadening of pore size distributions (PSD) accompanied by enhancement of connectivity with increasing maturation degree (Valenza et al., 2013; Liu et al., 2023a).

2. Objectives

The reason for the study on the microstructure evolution in shale lies in the storage spaces and flow channels for the fluid hydrocarbon products it provides, which is key for shale oil recovery efficiency (Tiwari et al., 2013). However, the products formed inside OM create secondary pores and their chemical, physical, and flow characteristics affects the flow pathways in turn (Zhong et al., 2013; Wang et al., 2015b, 2016; Ardakani et al., 2018). Tiwari et al. (2013) reported that the generation and expulsion of movable hydrocarbons transform the impermeable media to permeable porous media in the Green River shale, and several complex physical and chemical changes have also been recognized during the thermal conversion of OM. The thermal maturation of shale actually involves the simultaneous evolution of the pore system, rock fabric, and fluid products, it is critical to clarify the evolutions of geochemical and geophysical properties and their interactions for a better understanding of the pyrolysis behaviors of shale. Therefore, a combined investigation on the simultaneous evolution of petrophysical and chemical properties is required in the study of artificial maturation of shale.

In this work, stepwise hydrous pyrolysis was applied with subsequent geochemical analysis, including the quantification on the liquid and gaseous products, compound group (saturates, aromatics, non-hydrocarbons, asphaltenes) separation on the liquid products, TOC, Rock-Eval, and Ro measurements on the solid matrix, and petrophysical measurements involving X-ray CT and LTNA on the shale solid. The original samples and the solid residues after pyrolysis were characterized geochemically by TOC, Rock-Eval, Ro measurements and petrophysically by X-ray CT and LTNA. The liquid products remained inside solid residues were measured by compound group separation and quantification after solvent extraction. The samples selected for this study were lacustrine organic-rich carbonaceous shales from the Lucaogou formation in the Jimsar sag of Junggar Basin. The simultaneous geochemical and petrophysical changes of the samples during hydrous pyrolysis were investigated to reveal mechanisms of the complex chemical and physical interactions during thermal maturation. This work is thought to provide a deeper understanding of the simultaneous evolution of geochemical and petrophysical properties of carbonaceous shales upon in-situ subsurface retorting, which may provide useful guidance for the geologists and engineers for site selection and process optimization.

3. Geological setting

The study area, Jimsar sag, is located in the south-east of Junggar Basin, the largest superimposed sedimentary basin of China. The sag has a great shale oil potentials with estimated geological hydrocarbon resource of 15.8×10^8t (Carroll et al., 1990; Cao et al., 2005, 2016). It is a half graben-like depression with an eastern up-dip, whose western margin is controlled by faults and the eastern margin is stratigraphically overlapped (Fig. 1A). The thick fine-grained organic-rich carbonaceous sediments of Lucaogou formation in the sag, including mudstone, siltstone, dolomite limestone, and tuff, are the most prospective oil-bearing strata, where two shale oil "sweet spots" have been identified in the upper ($P_2l_2^2$) and lower ($P_2l_2^1$) sub-sections (Fig. 1 B)(Cao et al., 2016; Hackley et al., 2016; Zhang et al., 2018; Ding et al., 2019; Pang et al., 2022).

In contrast to the marine argillaceous oil shale plays in the USA, the Lucaogou shales were deposited near the coast of saline lake. It consists of a mixture of carbonate and siliciclastic minerals owing the terrestrial provenance and fluctuating lake levels, showing distinct geochemical and petrophysical properties with common argillaceous shale (Fig. 1 C–J) (Wu et al., 2016, 2021; Zhen et al., 2016; Pang et al., 2018). The Lucaogou shale was chosen for its special petrographic features and because it contains mixed lacustrine fine-grained organic-rich sediments typical for China. These occur in the Cangdong depression in the Huanghua Sag and the Dong Ying depression in Jiyang Sag, Bohai Bay Basin (Li et al., 2015; Wang et al., 2015a; Yong et al., 2016; Liu et al., 2019; Wang et al., 2019). Therefore, study on this type of lacustrine shale is expected to provide valuable information for current shale oil research in China.

4. Samples

The samples were taken from freshly drilled carbonaceous shale cores of the lacustrine Lucaogou formation (P_2l_2 member) in the Jimsar

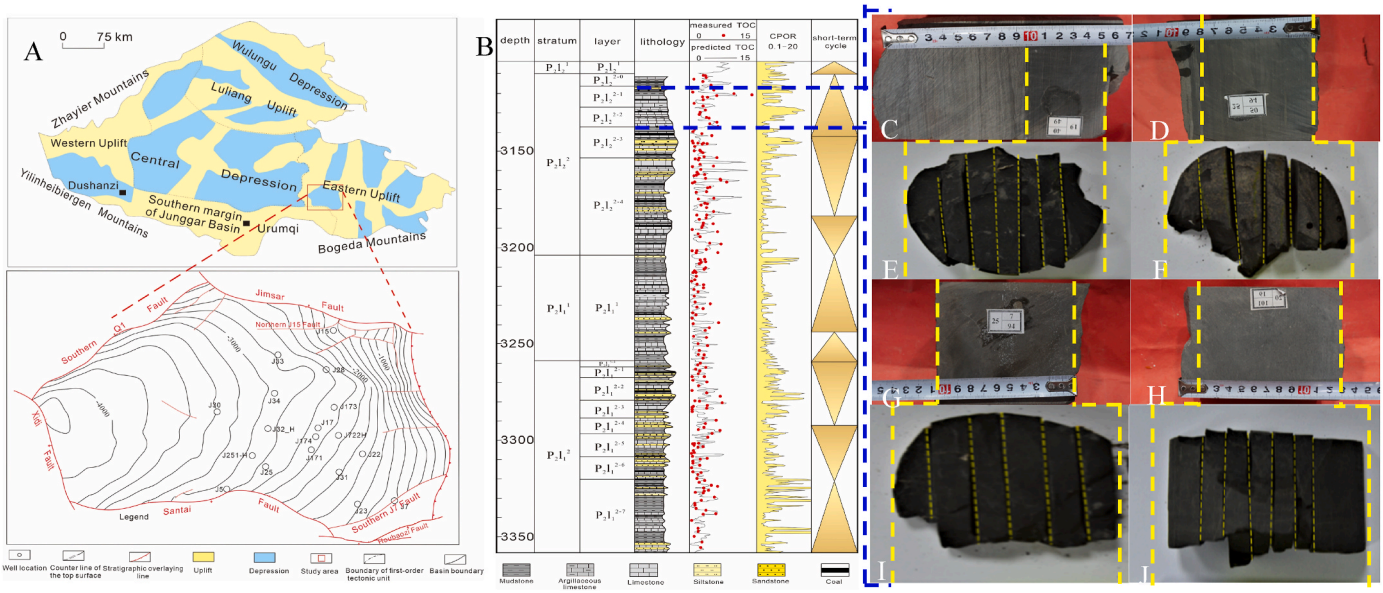

Fig. 1. (A) Location of the Jimsar sag in the Junggar Basin, China with top surface contour map of the Permian Lucaogou formation; (B) Stratigraphic columns showing the sampling intervals of the four representative carbonaceous shales. Photographs on the right show the samples before and after cutting of the sub-samples used in the hydrous pyrolysis experiments. Sample 1: thin laminae (C and E); Sample 2: thick laminae (D and F); Sample 3 unlaminated massive shale with high clay content (G anmd I); Sample 4: unlaminated massive shale with low clay content (H and J).

Sag, Junggar Basin, China (Fig. 1 A and B). Two samples came from the upper subsection ($P_2l_2^2$), and the other two from the lower subsection ($P_2l_2^1$). After initial geochemical screening of eight cores, four samples exhibiting similar basic geochemical properties in terms of kerogen type (liptinite-dominated, type I), TOC values (5.0 %–7.5 %), and thermal maturity (vitrinite reflectance Ro: 0.69–0.80 %), and Rock-Eval parameters (S_1: 1.97–3.22 mgHC/g; S_2: 14.93–40.04 mgHC/g) were selected. Thus, the influence of the OM was eliminated to a large extent so that the effects of rock fabric on the generation and expulsion of petroleum and the evolution of the petrophysical properties during thermal maturation could be studied.

Depths, lithotypes, and organic geochemical and mineralogical compositions of the four samples are listed in Table 1 and images of the samples and sub-samples are shown in Fig. 1. The specific rock fabric features of the individual samples are as follows.

- Sample 1 (2541.4 m): Thinly laminated quartz-rich mudstone with laminae thickness <1 mm (>10 laminae per cm)
- Sample 2 (2295.5 m): Laminated mudstone with laminae thickness >1 mm (<5 laminae per cm)
- Sample 3 (2298.4 m): Massive mudstone with low TOC and high feldspar and clay contents (not laminated)
- Sample 4 (2853.9 m): Massive mudstone with high feldspar and low clay contents (not laminated)

5. Experimental methods and procedures

Hydrous pyrolysis was used to simulate the thermal maturation of the low-mature shale samples. The original samples and the solid residues after each individual pyrolysis steps were analyzed geochemically by applying the Rock-eval pyrolysis, vitrinite reflection ratio measurement, and TOC analysis, and their microstructure was investigated using image analysis of X-μCT and petrophysical method of LNTA to obtain the full-range pore structure information, of which the X-μCT can provide the structure information for the pore spaces >1 μm and the LNTA provides the information of pores <1 μm. The liquid and gaseous products and extracts from the solids were analyzed by standard geochemical methods, including the gaseous and liquid products quantification and compound group analysis of liquid petroleum by liquid chromatography. A scheme of the experimental and analytical workflow is shown in Fig. 2.

5.1. Hydrous pyrolysis experiment

Hydrous pyrolysis experiments were conducted using the GPM-3 closed system pyrolysis reactor at the State Key Laboratory of Petroleum Resource and Engineering of China University of Petroleum, Beijing. The unit consists of an autoclave vessel, equipped with a temperature-programmable heating system, a vacuum pump, and temperature and pressure sensors. The maximum temperature of the reactor is 600 °C and the maximum fluid pressure 50 MPa.

Slabs of the shale cores (approximately 1 cm thick) were cut into six prism-shaped pieces of approximately equal weight (~50 g, Fig. 1 E, F, I, J). Each piece was placed into a high-pressure reactor vessel and submerged completely in the distilled water (10 ml–30 ml) to simulate the pyrolysis behaviors with water in the actual shale intervals in the Lucaogou formation. The reactor vessel was then closed, evacuated, pressurized with N_2 to 30 MPa and leak-tested before starting heating program. Hydrous pyrolysis was conducted at five individual temperatures, 295, 320, 345, 370, and 400 °C for 24 h, following the protocols used by Berner and Faber (1996), Behar et al. (1997), Tiwari et al. (2013), Chen and Xiao (2014), and Liu et al. (2023a).

5.2. Analytical procedures

5.2.1. Organic-geochemical characterization

The total organic carbon (TOC) content of the original samples and the pyrolyzed solid residues were determined using a LECO CS-230 instrument. The samples were ground to 80 mesh, treated with 5 % dilute hydrochloric acid to remove carbonates, then washed with distilled water and dried for 24 h. Rock-Eval analysis was conducted on the dried samples grinded to 60–80 mesh using a Rock-Eval 6 analyzer. The grinded samples of ~100 mg is placed into the oven and then the oven is kept isothermally for 3 min at 300 °C, upon which the free hydrocarbons are volatilized from the rock and measured as S_1 by the detection of the FID. The temperature rises from 300 °C to 550 °C with an increasing rate of 25 °C/min, whereby the volatilization of heavy hydrocarbon compounds as well as cracking of organic matter happens. The released

Table 1
The Basic geological and geochemical information for the samples.

Sample ID	Depth/m	Lithology	Ro/% (measured)	TOC/%	S1/mgHC/g	S2/mgHC/g	Tmax/°C	HI mg/gTOC	Quartz/%	Feldspar/%	Clay minerals/%	Calcite/%	Dolomite/%	Pyrite/%	siderite/%	glauberite/%	Aragonite/%	Augite/%
1	2541.40	Thin laminated mudstone	0.75	5.27	3.22	31.26	446	592.83	34.40	5.5	27.8	4.4	15.5	1.6	1.3	9.5	/	/
2	2295.50	Thick laminated mudstone	0.69	6.12	2.82	35.93	443	587.48	23.60	3.7	45.8	19.4	/	/	/	/	7.5	/
3	2298.40	Massive mudstone	0.71	1.93	1.97	14.93	446	598.16	/	12.5	56.7	/	18.1	/	/	/	/	12.7
4	2853.90	Massive mudstone	0.80	7.58	2.20	40.04	445	528.02	27.00	15.6	31.1	7.2	17.0	/	2.1	/	/	/

hydrocarbon from this phase is measured as the S_2 peak by FID, especially the high S_2 values are checked with the FID signals and the values and signals are in reliable limits. The T_{max} is identified at which S_2 reaches its maximum. The trap of CO_2 in the 300 °C to 390 °C range is heated to release the CO_2 and the CO_2 is detected on a TCD during the cooling of the oven, which is measured as S_3 peak (Lewan, 1994; Lewan and Ruble, 2002; Carvajal-Ortiz and Gentzis, 2015; Hazra et al., 2017; Hazra et al., 2019). Thin sections prepared from the slices cut from the solid samples were dried for 12 h and were then observed by the Zeiss scope 5 microscope facilitated with microspectrophotometer to determine the vitrinite reflectance (Ro). The measurement follows the testing standard SY/T5124-2012 of China and the reflectance ration was derived on 50 points after a standard calibration.

5.2.2. Analyses of gaseous products, expelled bitumen, and retained bitumen in solid residues

After each hydrous pyrolysis experiment, the gaseous products were collected and analyzed using an Agilent 7890 chromatograph and 5975c mass spectrometer. The expelled petroleum was extracted from the aqueous phase using dichloromethane and was then separated into compound groups (saturates, aromatics, non-hydrocarbons, asphaltenes) by liquid chromatography. Aliquots of the solid residues were mechanically crushed to 100 mesh, and solvent-extracted using a 98:2 chloroform chloroform/methanol mixture. The extracts were separated into compound groups (saturates, aromatics, non-hydrocarbons, asphaltenes) by liquid chromatography.

5.2.3. Porosity and pore size distribution

The porosity of the original solids before pyrolysis and unextracted pyrolyzed solid residues was measured by LTNA and X-ray CT. For the LTNA, the (unextracted) samples were powdered to 60–80 mesh and dried at 60 °C for 12 h. Measurements were performed with an ASAP 2020 specific surface area analyzer. Adsorption isotherms (up to P/P0 of ~0.95) and desorption isotherms were recorded at 77 K and processed. The pore size distribution (PSD) in the range from 1.7 nm to 200 nm was determined using the Barrett-Joyner-Halenda model.

X-ray CT was performed on a Zeiss Xradia Versa 510 X-ray computed tomography instrument with a maximum resolution of 1 μm. The three-dimensional spatial distribution of pores and their detailed pore and throat parameters were derived from digital core analysis on hundreds of grayscale images by applying the FEI AVIZO Fire 9.0.1 Graphic Software. Pore system was extracted from rock matrix by image segmentation following the grayscale interactive threshold methods and then porosity was calculated by volume fraction model. The segmentation porosity was compared with the filed test results in the same depth to eliminate the personal error, and then the pore network modelling was conducted on the extracted pore system, by which PSD in the size range of 1 μm–500 μm was obtained.

The two methods yield complementary porosity values, of which the X-ray CT describes the macropores and fractures >1 μm, and LTNA detects the sum of the micropores, mesopores, and part of the macropores (Chalmers et al., 2012; Clarkson et al., 2012, 2013; Gou et al., 2019; Qiao et al., 2020a,b, 2022; Arif et al., 2021). Here we define the CT porosity as “macroporosity”, LNTA porosity as “microporosity”, and the sum of the two as total porosity.

6. Results

6.1. Organic geochemical evolution of the shales during thermal maturation

6.1.1. Vitrinite reflectance, TOC and Rock-Eval parameters

The evolution of the organic geochemical parameters of the four shale samples upon artificial maturation is shown in Fig. 3 and Table 2. With increasing pyrolysis temperature, the R_O of the shale samples increases continuously, and the TOC decreases due to conversion of OM

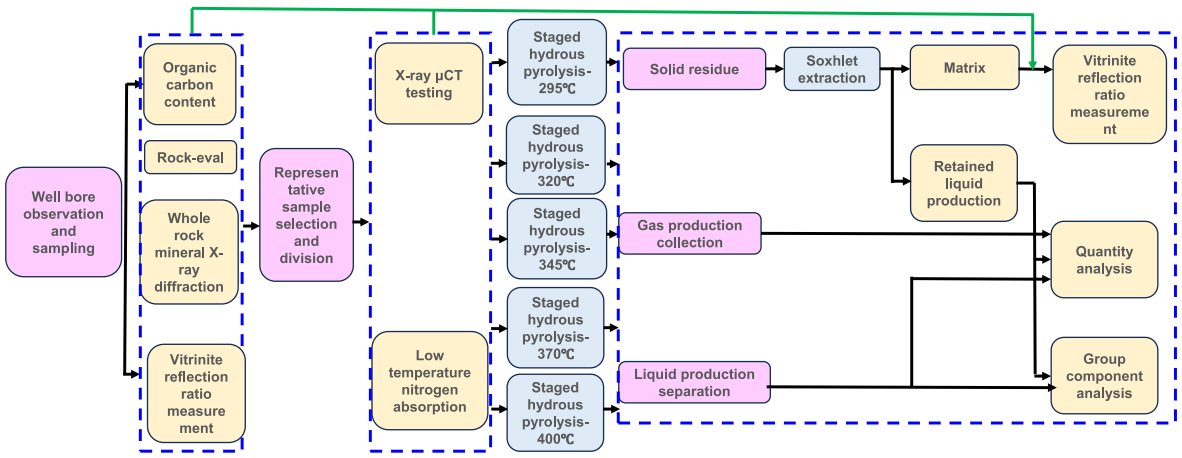

Fig. 2. Experimental and analysis workflow for the investigation of the coupled geochemical and petrophysical evolutions during the artificial maturation (24 h at 5 different temperatures).

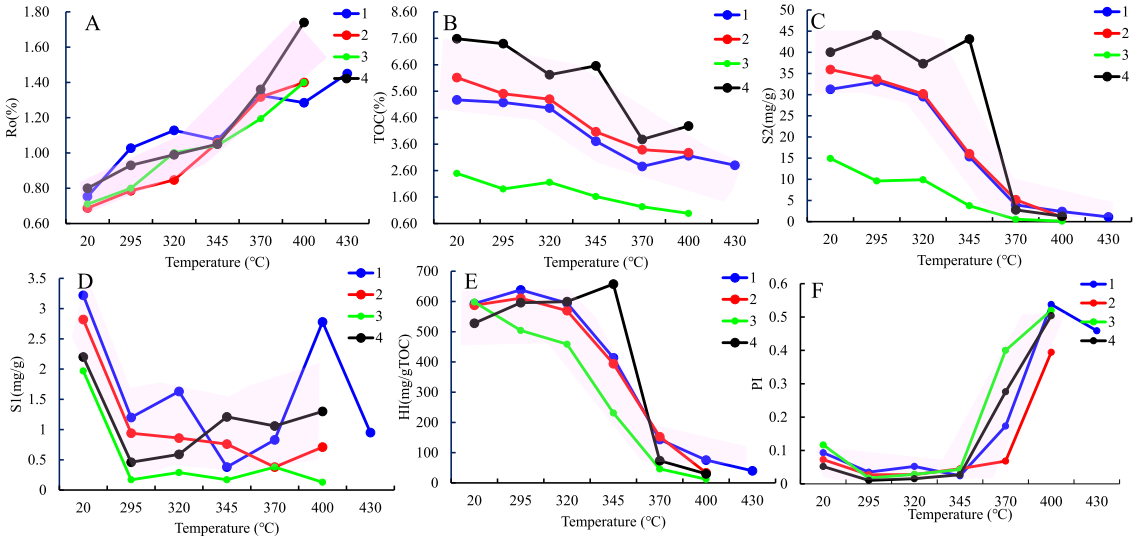

Fig. 3. Evolution of organic geochemical parameters of the solid residues of the four different lithotypes after hydrous pyrolysis at different temperatures. (A) Vitrinite reflectance (Ro), (B) Total organic carbon content (TOC), (C) Rock-Eval S2, (D) Rock-Eval S1, (E) Rock-Eval Hydrogen Index (HI), (F) Production Index (PI). Samples 1 and 2 are mudstones with thick and thin lamina, respectively, and samples 3 and 4 are massive (non-laminated) mudstones.

and expulsion of the pyrolysis products at the same time (Fig. 3 A and B). The Rock-Eval S_2, and its related, TOC-normalized parameter HI, decrease rapidly from 320 to 370 °C (Fig. 3 C and E), indicating the phase of peak oil generation (transformation of OM) associated with the decrease of the remaining petroleum generation potential. The evolution trends of TOC, S_2, and HI agree well with the published hydrous and anhydrous pyrolysis results of the organic matter rich shale with type I and II_1 kerogen in the Qingshankou formation in the Songliao Basin, Green River formation in the Uinta Basin and Piceance creek Basin, and Shahejie formation in the Bohaibay basin (Lewan and Ruble, 2002; Lewan et al., 2006; Ruble et al., 2001, 2003; Curry, 2003; Wang et al., 2022; Liu et al., 2023a). Besides, the results indicate that the TOC of the laminated samples decreases more rapidly than that of the massive one, and the transformation rate correlates with the intensity of lamination and the content of the rigid grains, quartz and feldspar. The shale with massive structure has a hysteresis in the reductions of TOC and HI in the beginning (Fig. 3 B). The shale with thin lamina exhibits great S_1 increases at 320 °C and 400 °C. The lower S_1 values of shale with massive structure probably indicate a moderate hydrocarbon release process than shale with laminations (Fig. 3 D).

The ratio of $S_1/(S_1+S_2)$, namely, PI, stays at low levels around 0.03 before 345 °C (Ro = 1.0 %) but rises sharply in the mature to high-mature stage (345 °C–400 °C, Ro 1.0 %–1.8 %) (Fig. 3 F). The TR, calculated by Eq. (1), shares similar trends, quite similar to the pyrolysis trends of type I and II_1 kerogen, Woodford shale, 72 h experiments of the Mahogany shale and black shale in Green River formation and their predicted results using the Arrhenius equation by applying the Mahogany pyrolysis parameters, and recent pyrolysis investigations on the lacustrine shale in the Qingshankou formation in the Songliao Basin and Shahejie formation in the Bohaibay Basin (Ruble et al., 2001; Amrani et al., 2005; Vandenbroucke and Largeau, 2007; Behar et al., 2010; Li et al., 2018; Wang et al., 2022; Lei et al., 2021).

$$TR = \frac{700 - HI}{700} \times 100\% \quad (1)$$

Where TR is the transformation ratio, %; HI is the hydrocarbon generation potential, mg/gTOC; 700 is the constant HI for organic-rich shales bearing type I kerogen.

6.1.2. Petroleum generation

The total generated petroleum (TGP), comprising the petroleum

Table 2
Geochemical and geophysical parameters during the thermal maturation.

Sample	Pyrolysis temperature/ °C	Ro/ %	TOC/ %	Total porosity/ %	Permeability (D)	S1/ (mg/ g)	S2/ (mg/ g)	Tmax/ °C	HI/ (mg/ gTOC)	ELP/ (mg/ gTOC)	RLP/ (mg/ gTOC)	Gaseous products/ (mg/ gTOC)	TLHG/ (mg/ gTOC)	THG/ (mg/ gTOC)
1	20	0.75	5.27	0.90	0.00042	3.22	31.26	446	592.83					
	295	1.03	5.18	2.33	0.0012	1.20	33.03	441	638.26	22.79	34.13	10.40	56.93	67.33
	320	1.13	4.97	2.46	0.0014	1.63	29.53	441	594.64	121.34	43.75c	14.42	165.09	179.51
	345	1.07	3.71	3.42	0.00076	0.38	15.35	440	413.75	159.11	51.86	52.96	210.97	263.93
	370	1.33	2.76	4.13	0.0017	0.83	3.96	437	143.63	289.90	64.23	149.51	354.14	503.65
	400	1.29	3.16	5.84	0.0028	2.78	2.39	370	75.56	319.34	97.99	278.19	417.33	695.53
	430	1.45	2.80	10.67	0.0018	0.95	1.12	581	39.97	20.90	9.94	486.56	30.83	517.40
2	20	0.69	6.12	1.23	0.00029	2.82	35.93	443	587.48					
	295	0.79	5.51	6.60	0.00071	0.94	33.62	438	610.72	48.47	48.08	19.57	96.55	116.12
	320	0.85	5.30	5.35	0.00154	0.86	30.18	440	569.54	65.95	98.08	29.76	164.03	193.79
	345	1.06	4.07	8.24	0.00059	0.76	16.03	442	394.15	266.66	23.90	50.09	290.56	340.66
	370	1.32	3.39	8.75	0.0015	0.38	5.18	438	152.80	495.63	41.19	106.66	536.81	643.47
	400	1.40	3.28	15.79	0.0015	0.71	1.09	545	33.28	185.63	35.71	231.88	221.34	453.23
3	20	0.71	2.50	3.30	0.00025	1.97	14.93	446	598.16					
	295	0.80	1.91	4.28	0.00056	0.17	9.61	440	504.20	19.46	38.69	/	58.16	58.16
	320	1.00	2.16	5.83	0.00077	0.29	9.90	445	458.76	73.40	45.06	/	118.47	118.47
	345	1.04	1.62	9.24	0.0018	0.17	3.75	440	231.20	287.59	61.89	/	349.48	349.48
	370	1.19	1.23	6.98	0.00086	0.38	0.57	437	46.23	81.99	59.63	/	141.62	141.62
	400	1.40	0.98	4.51	0.00070	0.13	0.12	564	12.21	127.43	27.78	/	155.21	155.21
4	20	0.80	7.58	1.64	0.00027	2.20	40.04	445	528.02					
	295	0.93	7.39	6.75	0.00053	0.46	44.09	441	595.97	12.26	33.30	19.63	45.56	65.19
	320	0.99	6.22	3.11	0.0013	0.59	37.31	439	599.45	94.75	41.01	4.05	135.76	139.81
	345	1.05	6.56	4.44	0.0032	1.21	43.13	442	657.47	173.43	19.38	58.24	192.81	251.05
	370	1.36	3.78	8.07	0.0017	1.06	2.78	435	73.56	379.95	57.08	101.32	437.03	538.35
	400	1.74	4.29	6.56	0.00066	1.30	1.28	349	29.87	133.11	37.02	271.76	170.13	441.89

retained inside the rocks, the expelled liquid petroleum, and expelled gas products, increases with temperature, reaching a maximum between 345 and 370 °C (Fig. 4). The overall trend is similar to the hydrocarbon generation variations of the pyrolysis performed in the open system but show little differences with the results derived from the closed system and have discrepancies when the pyrolysis temperature is over 400 °C (Ruble et al., 2001; Behar et al., 2010). Compared with the decrease of TOC, the generation and expulsion of petroleum is slightly delayed (Fig. 4). The total amount of generated petroleum correlates with lamina density (Fig. 4A–C). From the shale with thin lamina to the one with thick lamina and to the massive one, the peak generation value successively decreases from 695 mg/gTOC to 349 mg/gTOC. The high hydrocarbon generation quantity suggests the presence of a type II-S kerogen with high bitumen content in the Lucaogou shale according to the laboratory measurements from Amrani et al. (2005) and Rosenberg et al. (2017).

Although the massive, unlaminated sample 4 has the highest TOC, it generates much less petroleum than sample 1 characterized by a lower TOC. Lamination promotes the hydrocarbon generation and expulsion (Fig. 4 A–D), in other words, the high rigid mineral content benefits the chemical reaction of organic matter and the migration of the pyrolyzed products. For the massive shale, the hydrocarbon generation rate rises

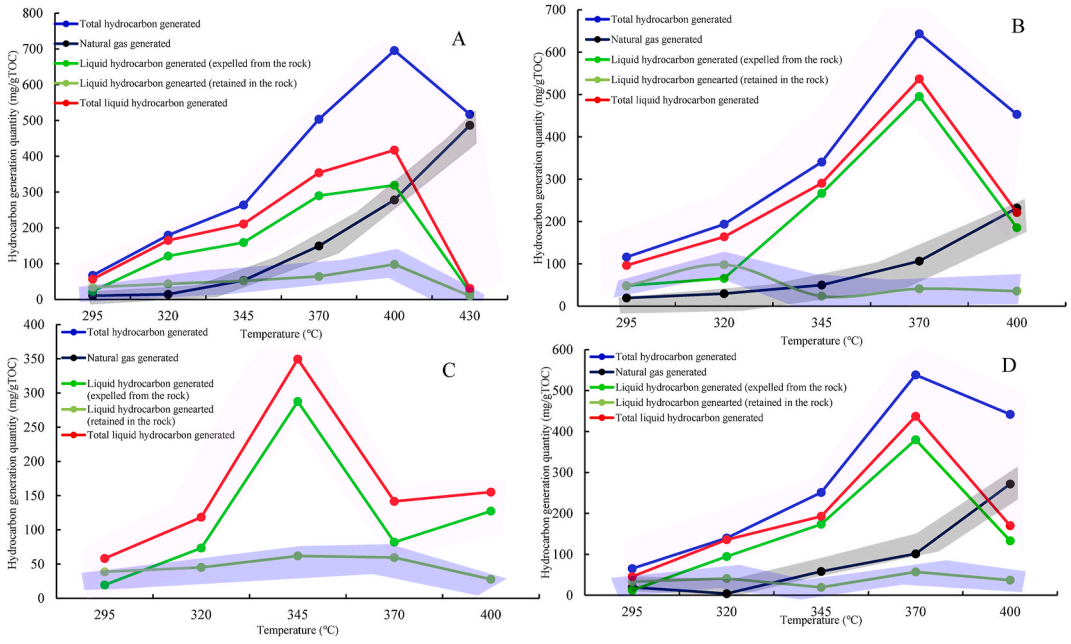

Fig. 4. Quantities of liquid and gaseous products generated during hydrous pyrolysis of the four shale samples. (A) mudrock with thin laminae (sample 1), (B) mudrock with thick laminae (sample 2), (C) massive, unlaminated, low-TOC mudrock (sample 3), and (D) unlaminated mudrock (sample 4).

along with the decreases of massive OM content, e.g. sample 3 (Fig. 3 B and 3 C).

The production patterns of the liquid petroleum (LP) are similar to those of the TGB, sharing similarities in the quantity and trend of the immiscible oil generation in the temperature range from 195 °C to 350 °C reported in the pyrolysis experiments conducted on the shales in Green River formation and Xiamaling formation (Huizinga et al., 1988; Lewan, 1994; Ruble et al., 2001; Li et al., 2018), but exhibit a sharper reduction in the high-mature stage owing to the thermal cracking of oil, which has also been reported in the high to overmature stage in the Ghareb Formation in the Golan Basin (Rosenberg et al., 2021). The natural gas shows a continuously increasing trend (Fig. 4) and the generated quantity is similar to the shale in Xiamaling formation of Bohai Bay Basin but a little higher than the Mahogany shale in the Unita Basin at same temperature (Ruble et al., 2001; Li et al., 2018). The quantity of the generated LP is close, while that of the natural gas varies significantly (Fig. 4 A–C). The thinly laminated shale generates more gaseous product per unit mass, and the gas to liquid (G/L) ratio increases sharply with thermal maturation, a little higher than the current reported results of the lacustrine and marine shale (Ruble et al., 2001; Li et al., 2018; Rosenberg et al., 2021). The sample with the thick laminae and the massive non-laminated samples have lower G/L ratios and is close to the published results in the shale with type I and II_1 kerogen (Ruble et al., 2001; Behar et al., 2010; Li et al., 2018). The different evolution patterns of G/L, which are characterized by an increasing trend in the thin lamina shale, an abrupt rise in the high-mature stage in thick lamina one, but a fluctuated increasing trend in the massive one, indicating different ways of hydrocarbon generation and expulsion in shale with different lamina structures (Fig. 4).

The quantities of expelled liquid product (ELP) and the pyrolysis product retained in the rock (RLP) were determined separately. The massive expulsion of the LP occurs from 345 to 370 °C, consistent with the massive immiscible oil generation in this temperature range reported by Ruble et al. (2001), but the RLP is lower than the bitumen measured in Mahogany shale (Ruble et al., 2001) (Fig. 4). Moreover, the results suggest that the four samples have different expulsion patterns.

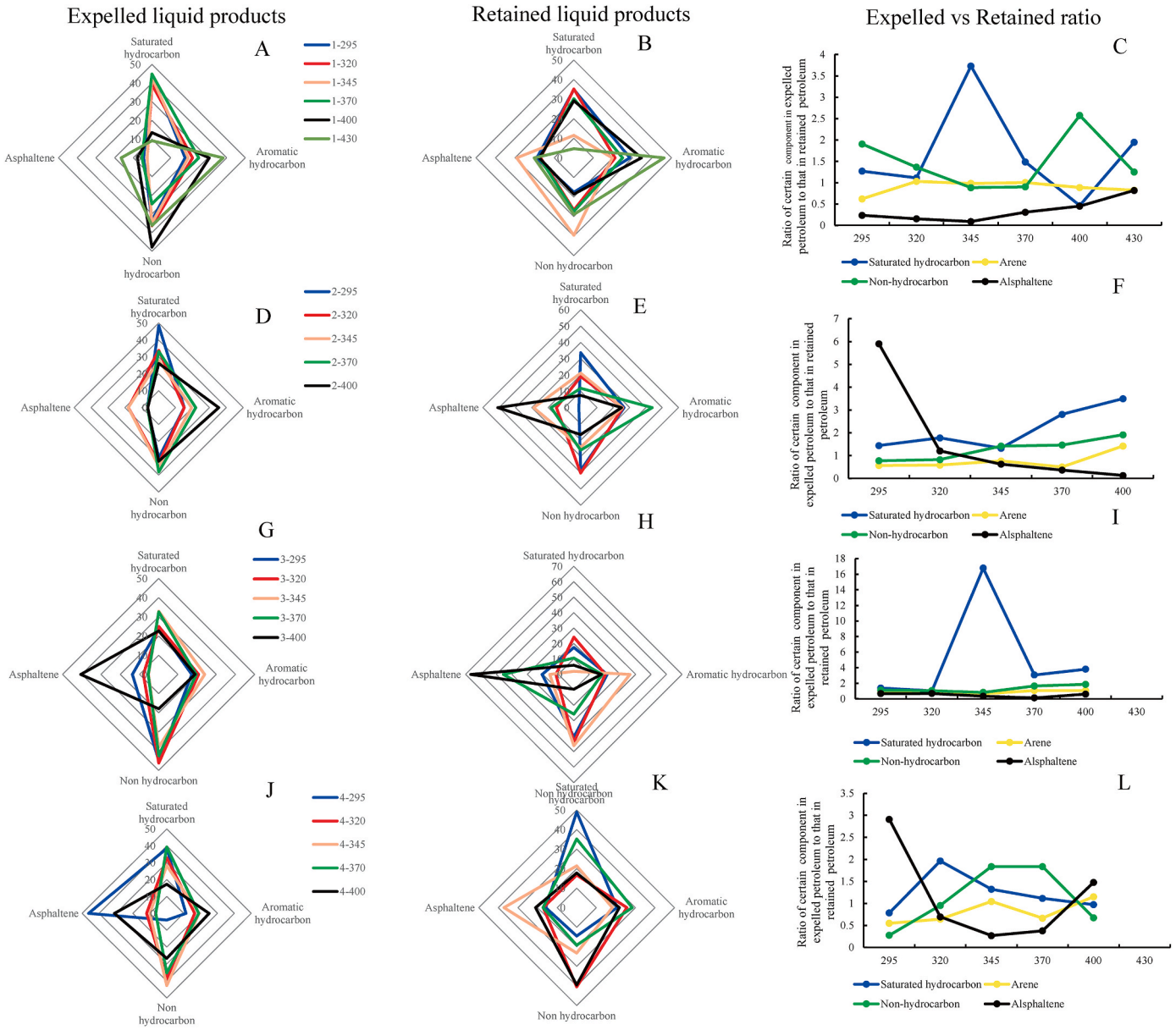

Fig. 5. Compound group compositions of the expelled liquid product (ELP; left column, A, D, G, and J), the retained liquid product (RLP; central column, B, E, H, and K), and the ratios of expelled vs. retained proportions of selected compound groups of the four shale samples (right column, C, F, I, and L) after thermal maturation.

Expulsion from the laminated specimen occurs immediately, while expulsion from the sample with thick laminae and from the massive fabric gradually accelerates, reaches a peak value and then declines. The ELP/LP ratio is around 0.9 in the thinly laminated shale, while those of the other three samples fluctuate around ~0.92. If natural gas is accounted, the expulsion hydrocarbon ratio of thin lamina shale reaches 0.98, however, it decreases to 0.82 in massive shale, indicating a stronger absorption in massive structure with relative higher content of clay minerals.

6.1.3. Chemical composition evolution of the liquid pyrolysis products

The results of the compound group analysis show the chemical evolution differences in the extractable (ELP) and retained (RLP) liquid products of the shales with different rock fabric during thermal maturation (Fig. 5). From low-maturity to mature stage, the ELP of the laminated shale is dominated by saturated hydrocarbons, while aromatic hydrocarbons prevail at high-maturity levels (Fig. 5 A), and this is similar to the compound group contents of the immiscible oil and bitumen generated at the end of the pyrolysis of Mahogany shale and Green River shale (Ruble et al., 2001, 2003; Curry, 2003). The asphaltene contents exhibit complex variations in ELP in shale with different laminated structures, that of thin laminated one increases with pyrolysis temperature, the thick laminated one has an increasing to decreasing trend and is close to the fractional composition variation of the yields in Green River shale, and the massive shales show decreasing to increasing trend (Ruble et al., 2001; Curry, 2003). The non-hydrocarbon percentage decreases in the 295 °C–370 °C temperature range and increases afterward.

For the RLP, the saturated hydrocarbon content decreases from mature to high-mature stage, and the non-hydrocarbon content is lower than expelled products, reaching its peak at 345 °C. The aromatic hydrocarbon content is higher and shows an increasing trend, and the asphaltene content is at around 20 %, greater than that in ELP, and has an increasing trend before 345 °C and then decreases afterward (Fig. 5 B). Asphaltene contents of thick laminated and massive shale in RLP at the end of pyrolysis are consistent with that reported in Mahogany shale (Ruble et al., 2001; Curry, 2003), while that of the thin laminated one is much lower. The aromatic content keeps stable or has a slight increment with the rising maturation in ELP and a weakly increasing trend in RLP. This phenomenon indicates a blockage for the heavy compounds of liquid petroleum expulsion in the low mature to mature stage.

The aromatic hydrocarbon content in the ELP of the sample with thick lamination is 4 % less than the one with thin lamination on average, while asphaltene content is 4.5 % higher (Fig. 5 D). The asphaltene is much greater in the RLP of the sample with thick lamination, dominating the retained products with percentage of 50.88 % in high mature stage (Fig. 5 E). The saturated hydrocarbon content in the expelled products of the massive shales is lower and fluctuates, while the content of asphaltene is greater (Fig. 5 G–J).

The ratios of the four group component contents of the ELP to RLP were calculated separately, and the results indicate that the expulsion of flexible light component follows the decomposition of OM, reaching its peak in mature stage (345°C–370 °C). However, the heavy ones do not follow, which shows different expulsion patterns in shale with different lamination (Fig. 5C–F, I, L). The ratio of asphaltene increases with the rising temperature in thin lamination shale but decreases in the thick lamination and massive samples (Fig. 5 C–F), of which the massive shales exhibit slight U shape owing to the asphaltene expulsion increment in high-mature stage (Fig. 5 I–L). The ratio of aromatic hydrocarbon keeps stable and that of the non-hydrocarbon increases with maturation, in which the increment in thin lamination shale is higher (Fig. 5C–F, I, L).

6.2. Petrophysical property evolution of the shales during thermal maturation

6.2.1. Porosity evolution

The porosity data for the shale samples after pyrolysis are listed in Table 2. Porosities of the laminated shales show a generally increasing trend with thermal maturation, exhibiting slight fluctuations, consistent with the with the porosity and pore volume evolutions of lacustrine Qingshankou shale, oil shale in the Upper Cretaceous Luozigou system, and shale in North American basin, and etc., during naturally and artificially thermal maturation processes (Chen and Xiao, 2014; Lei et al., 2021; Wang et al., 2022; Liu et al., 2023a, 2023b; Hazra et al., 2024). Starting from porosities around 1 %, the maximum porosity of the sample with thick laminae is 15.8 %, while the sample with thin lamina reaches a value around 11 % (Figs. 1 and 6 A and B). The initial porosities of the massive shale samples are higher (~1.5–3 %) and their increasing trends are not linear. The porosity trend of sample 3 (Figs. 1 and 6 C) exhibits one maximum and the trend of sample 4 (Figs. 1 and 6 D) has two maxima. These conspicuous differences in porosity evolution may be due to heterogeneities of the original cores. The maximum and final porosity values of massive shale samples are consistently less than 10 %. The overall evolution trend of the artificial maturation shows similarities with the field test data of in-situ retorting of the Fushun oil shale and Youwogan oil shale in Maoming Basin.

The porosity increase of the thinly laminated shale mainly originates from microporosity in the low-mature to mature stage (Ro 0.6 %–1.2 %), but is dominated by an increase of macro-porosity at the high-mature stage (Ro>1.2 %) (Fig. 6). Both macro-porosity and microporosity contribute to the porosity increment during the maturation process of the thickly laminated shale, of which the macro-porosity dominates the low mature and high mature stages and the microporosity dominates the mature stage (Figs. 1 and 6 B). In the massive shale, the microporosity determines the evolution of total porosity, which have also been reported by Chen and Xiao (2014) in the Upper Permian shale in the southeastern of Junggar Basin. However, the changes in macro-porosity also brings fluctuations to the porosity evolution, indicating the rising effects of fractures in high mature stage (Figs. 1 and 6 C and D). The origination of porosity increment of laminated shale is quite similar to the results reported in naturally and artificially thermal maturation of the lacustrine Qingshankou shale (Liu et al., 2023a, 2023b), and those of the massive shale are consistent with the results reported in shales in North American Basin, Baltic Basin, and Upper Permian outcrop of the southern Junggar Basin to some extent (Chen and Xiao, 2014; Kuila et al., 2014; Li et al., 2020).

6.2.2. Evolution of pore space based on LNTA

According to the 1985 IUPAC Manual on Reporting Physisorption Data for Gas/Solid Systems, hysteresis loops observed between the adsorption and desorption branches of LTNA measurements comprise four main types controlled by morphology (structure, shape, connectivity) of the pore system (Sing, 1985; Thommes et al., 2015).

The LTNA hysteresis loops of the shale samples studied here, evolve with the level of thermal maturation (Fig. 7). The four shale samples originally exhibit H_2 type hysteresis loops, which have also been reported by Chen and Xiao (2014) and Chang et al. (2022) in the low-mature to mature continental shale, but show different evolution patterns. Upon thermal maturation from low-mature to mature stage, the hysteresis loops change to the H_4 type with an increased offset between absorption and desorption curves. This is interpreted as a consequence of the generation of slit shaped pores and increase of the proportion of ink-bottle shaped pores. LTNA data from Liu et al. (2023a, 2023b) also suggested a H_4 type loops in the hydrous pyrolysis of the Qingshankou shale at 300 °C.

In the mature stages, the N_2 isotherms are characterized by H_3 type hysteresis, which is interpreted as an increase in macro-porosity and the formation of microfractures, agreeing well with the loop types of the

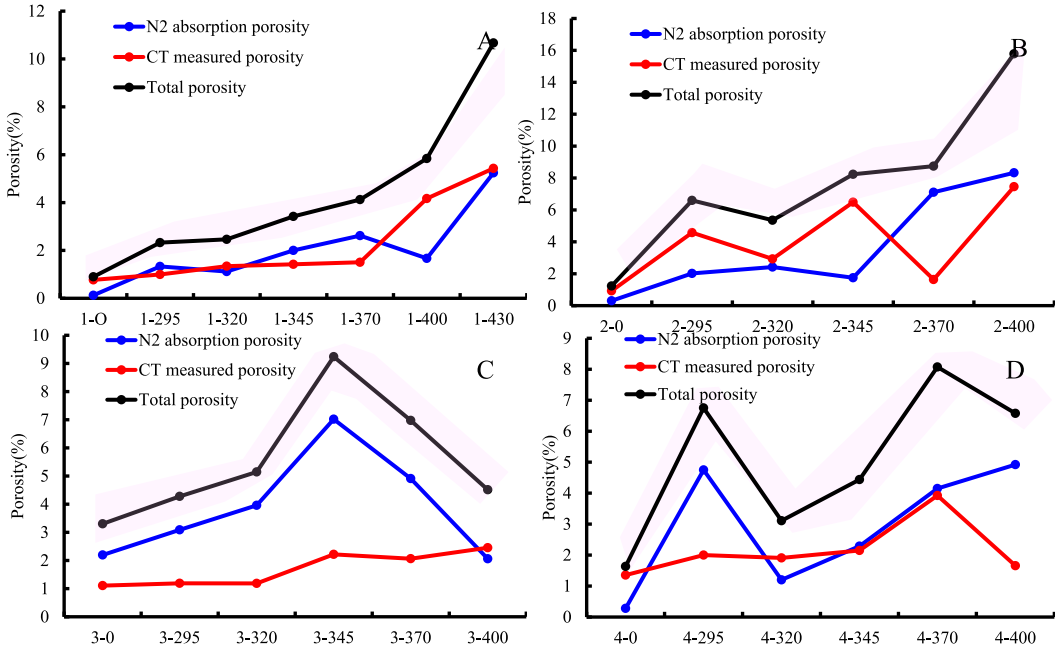

Fig. 6. The evolution of LTNA porosity, CT measured porosity, and the total porosity of the four samples (i.e. A. sample 1, B. sample 2, C. sample 3, and D. sample 4) during the thermal maturation process.

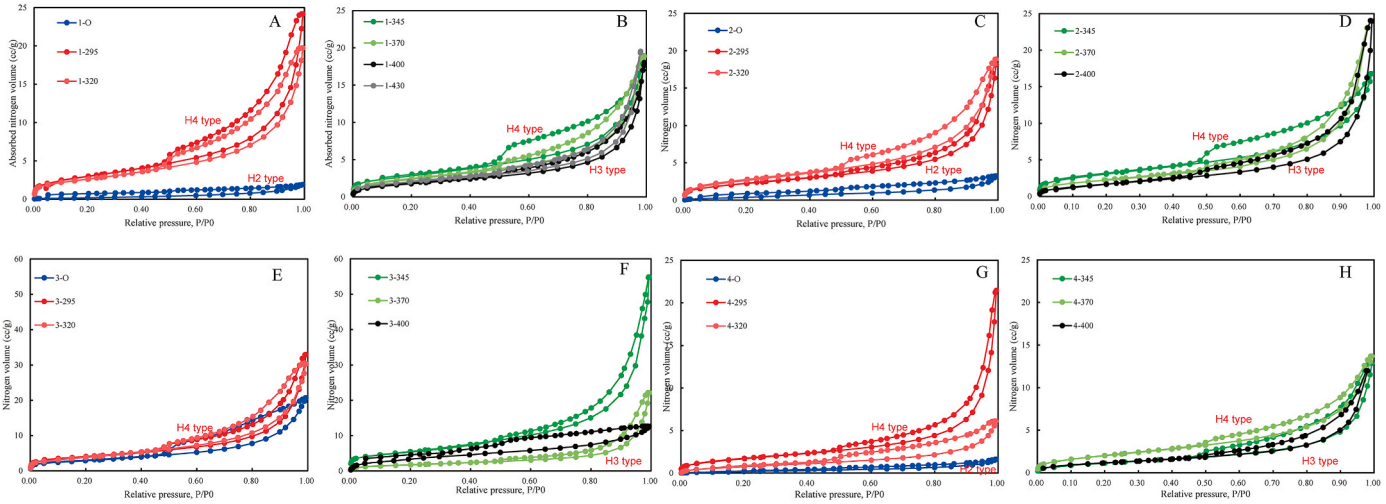

Fig. 7. The evolution of the hysteresis loops of the LTNA for the four samples (i.e. A and B. sample 1, C and D. sample 2, E and F. sample 3, and G and H. sample 4) during the thermal maturation.

mature to high mature Yaomoshan shale reported by Chen and Xiao (2014) (Fig. 7). The hysteresis loops of the samples with thick laminae and the massive samples show significant pore type changes after maturation at 345 °C - 370 °C (Fig. 7 C–H). The transition to the H_3 loop type hysteresis occurs earlier in the massive shales in the high-mature stage, closely associated with the generation of the microfractures (Fig. 7 E–H).

The results of the porosity evolution derived from the digital rock images in Figs. 8 and 9 are in good agreement with the interpretation of the LTNA data (Gou et al., 2019; Qiao et al., 2020a; 2020b, 2022). The CT data shows that the pore system consists of a large number of tiny spherical pores (500 nm-1 μm), some small-sized ink-bottle shaped pores (1 μm-50 μm), and a small number of relatively large-sized slit pores (>50 μm). In the laminated shales, the orientation of the pores is to some extent controlled by lamina, and there is a considerable proportion of slit pores. However, in the massive shales (Fig. 8), spherical and ink-bottle pores present without preferential orientation. With increasing maturation, numerous spherical pores form as a result of OM decomposition. The sizes of ink-bottle and slit pores increase in the low maturity stage, fresh microfractures forms in the mature stage and keep growing in the high mature stage, which have been previously observed in mature stage at 390 °C of Green River shale by in-situ pyrolysis monitored with X-μCT and synchrotron X-ray microtomography (Tiwari et al., 2013; Saif et al., 2016). Fresh spherical pores also expand with increasing maturation (Fig. 8 A–E) and they were not well-observed previously in Green River shale owing to the scanning resolution (Tiwari et al., 2013; Saif et al., 2016; Lei et al., 2021). In the massive shale samples, tiny spherical pores and ink-bottle pores form initially, followed by the generation of micro fractures upon transition from the mature to high-mature stage (Fig. 9 A–E). The micro fractures generated in the massive shales are finally healed as the pore pressure decreases and supporting rigid crystals are absent (Fig. 9), quite different from the

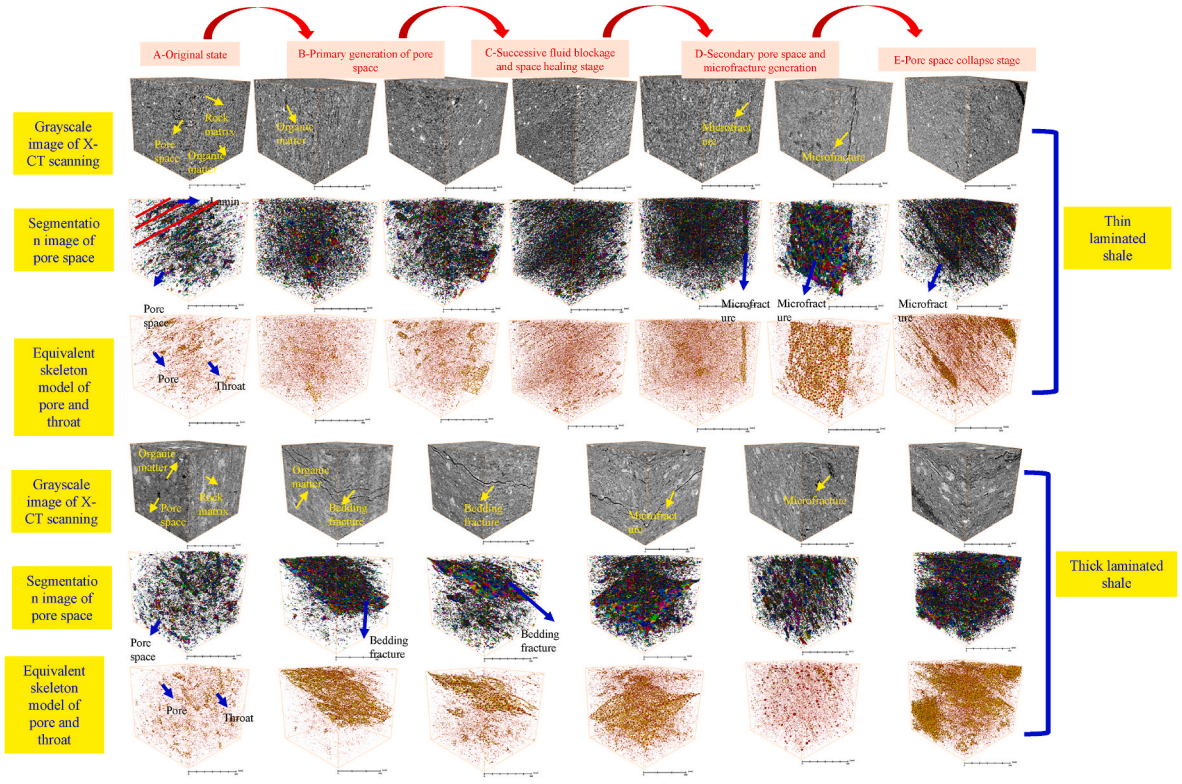

Fig. 8. The 3D digital rock images showing the evolutions of rock and matrix, pore system, and pore network model of the thin laminated sample 1 and thick laminated sample 2 during the thermal maturation. Note that the grayscale image shows the rock and matrix, the color labelled image displays the pore system and the connectivity of the pores, and the skeleton ball-stick image illustrates the pore system and the pore and throat configuration.

stabilization of the generated fractures during the 450 °C–500 °C in the X-CT imaging of Green River shale (Tiwari et al., 2013).

6.2.3. *Evolution of pore size distribution (PSD)*

The PSD from the integration of LTNA and X-CT suggests the volume increment is dominated by the pores with radii of 10–200 nm in the beginning and remains stable after heating to 295 °C and 320 °C (Figs. 10 and 11), and this trend is almost consistent with the results of Liu et al. (2023a, 2023b) reported in the pyrolysis of Qingshankou Shale. At higher maturity levels, porosity increases due to increment of pores in the 1 μm - 5 μm, and larger fractures with radii between 5 μm and 20 μm formed in the high-mature stage, agreeing well with the observation of Li et al. (2020) through the X-μCT conducted on the pyrolysis process of oil shale in the upper layer of the Cretaceous Luozigou System in Jilin Province, China. Furthermore, the number of pores with widths ranging from 50 nm to 1000 nm increases towards the end of pyrolysis (Figs. 10 and 11) and the PSD intend to be more disperse, which has also been observed by Wang et al. (2022). The increase of pores >1 μm occurs earlier and increase of pores of 10–1000 nm is less in the thick laminated than in the thin laminated shale (Fig. 10 A and B, F, 11 A, B). In massive shales, the proportion of pores >1 μm changes to a lesser extent and porosity increase is dominated by pores of 10 nm - 200 nm owing to the higher clay content in the rock matrix. The porosities undergo shrinkages above a temperature of 370 °C, evidenced by a collapse of pores and fractures (Fig. 10 C and D, Fig. 11 C and D). The variation is quite different from the reported continuously increasing trend of the micro-, meso, and macro pores.

6.2.4. *Evolution of absolute permeability*

Permeability determines the economic development of the shale oil and gas resources. However, the evaluation of permeability is difficult, aggravated by nanometer scale confinement and complex pore-fracture porous structure (Javadpour, 2009; Darabi et al., 2012; Gupta et al., 2018). Numerous models for permeability prediction have been proposed in shale gas research considering specific effects of gas transport in narrow pores, such as Knudsen diffusion, transitional flow, slip flow, and viscous flow (Rutherford and Do, 1997; Beskok and Karniadakis, 1999; Javadpour, 2009; Sakhaee-Pour and Bryant, 2012; Singh et al., 2014). Sakhaee-Pour and Bryant (2012) developed a polynomial model on the basis of models proposed by Beskok and Karniadakis (1999) and Javadpour (2009) that accounts for different flow regimes in a single straight cylindrical nanotube. The model modifies the viscous flow and suits for describing the dominant transition flow ($0.1<Kn<10$) in the fine-grained porous media, which can be expressed as follow.

$$K_a = \frac{\lambda^2}{32}\left(0.8435 + 5.4576\mathrm{K_n} + 0.1633\mathrm{K_n}^2\right) \tag{2}$$

The Knudsen number is defined as the ratio of the molecular mean free path (l) to pore diameter λ and can be expressed in Eq. (3), of which the l can be calculated in the following Eq. (4)

$$\mathrm{K_n} = \frac{l}{\lambda} \tag{3}$$

$$l = \frac{k_B T}{\sqrt{2}\pi\delta^2 P} \tag{4}$$

Where the k_B refers to the Boltzmann constant of 1.3805×10^{-23}/K, T is the temperature (K), δ is the collision diameter of gas molecule (m), and P is the pore pressure (Pa).

The λ for certain sized pores can be derived from the integrated PSD and their K_n can be calculated. The determination of the critical geometric length scale is a problem in shale since the mean pore length and mean pore radius cannot describe the pore system distributing from nanometer to millimeter well. Instead of mean or average parameter, we propose a critical flow length (CFL) by averaging the pore diameters of the peaks in the K_n range of 1 - 10 in the frequency distribution of K_n

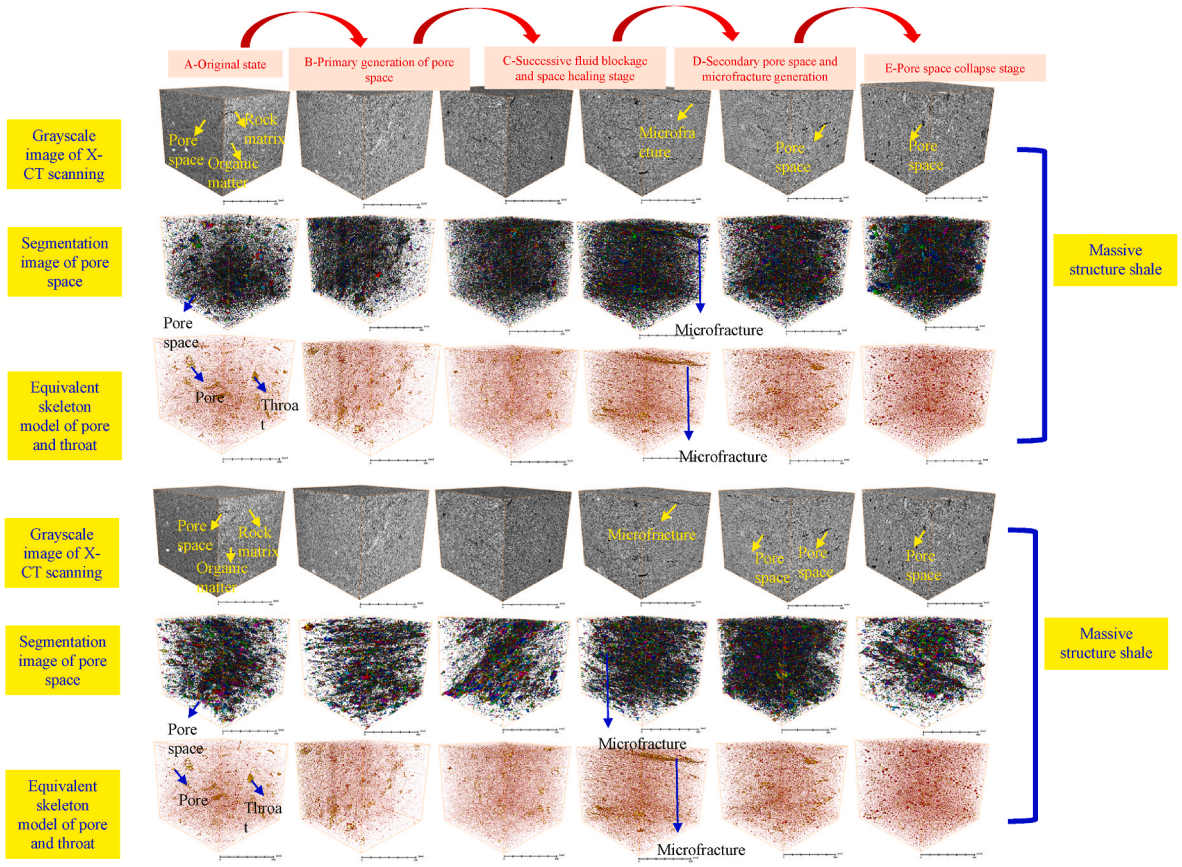

Fig. 9. The 3D digital rock images showing the evolutions of rock and matrix, pore system, and pore network model of the massive samples 3 and 4 during the thermal maturation. Note that the grayscale image shows the rock and matrix, the color labelled image displays the pore system and the connectivity of the pores, and the skeleton ball-stick image illustrates the pore system and the pore and throat configuration.

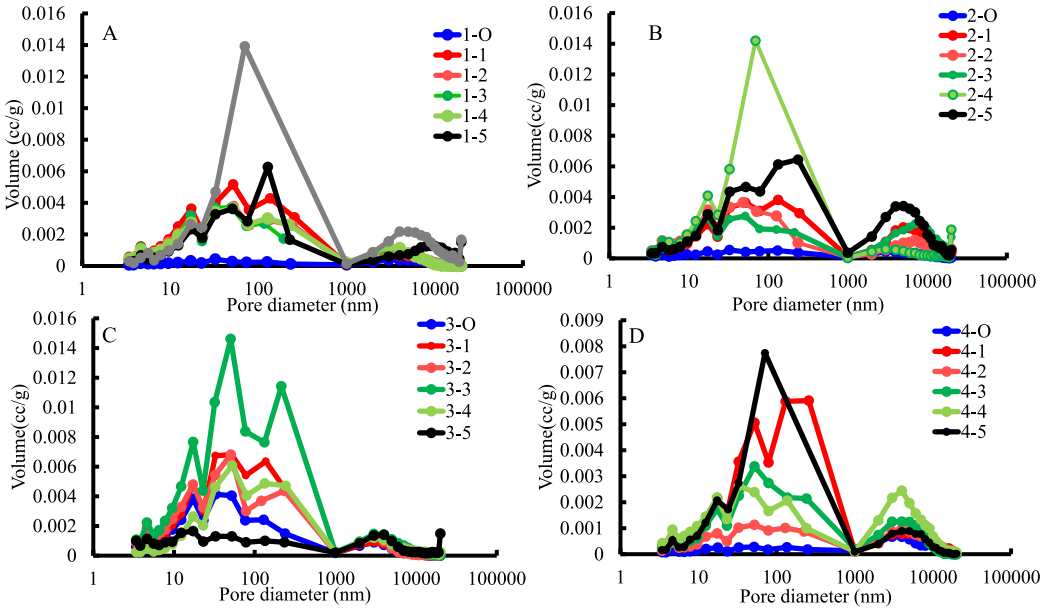

Fig. 10. The evolution of the pore size distribution derived from the integration of the LTNA and X-μCT during the thermal maturation (i.e. A. sample 1, B. sample 2, C. sample 3, and D. sample 4). Note that the numbered 1-1 represents the first pyrolysis stage of the sample 1 and the rest labelled number can be explained by that analogy.

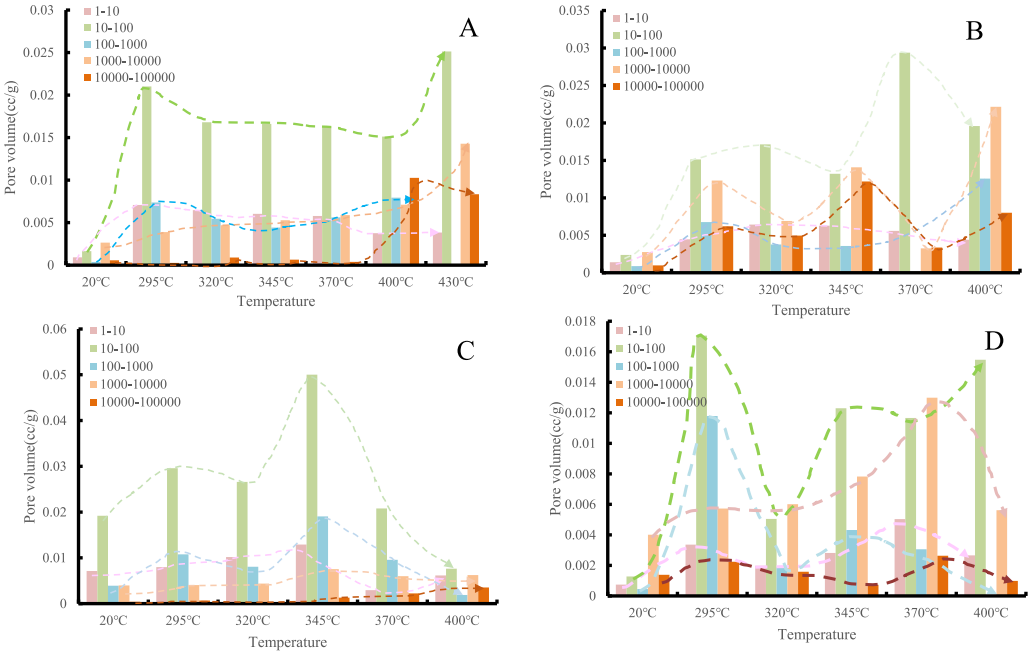

Fig. 11. The evolution of the pores in different size range during the thermal maturation (i.e. A. sample 1, B. sample 2, C. sample 3, and D. sample 4).

plot, and a representative K_n can be also obtained by averaging the peak value of K_n.

The permeability coefficients calculated are quite close to the value of North America Basin shale reported by Valenza et al. (2013) when the Ro is lower than 1.0 %, staying at several hundreds of nano Dacrys. They vary with the degree of thermal maturation, of which two continuous increasing to decreasing cycles can be identified (Fig. 12), and those are rarely reported due to the difficulties in measuring permeability of shale. The first increment presents in 295°C - 320 °C and then the decrease or stasis happens in 320°C–345 °C, which can be probably attributed to fluid retention. The secondary increment comes in high mature stage and the secondary decline occurs in 370°C - 400 °C owing to the space collapse associated with the reduction in the self-support induced by massive reaction and mass loss of OM (Fig. 12). The permeability at the mature to high mature stage is much greater than the value estimated in the current publications as most of the fractures and macropores are not well considered due to the detecting range of LNTA.

The evolution pattern differs in the massive and laminated shales, where the amplitudes of the first cycle are much greater in laminated shales, but those of the second cycle are lower than the massive shales, suggesting a greater pore loss in massive shale in high mature stage (Fig. 12 B). A delay presents in the permeability change of massive shales, suggesting a slow chemical reaction rate in the OM in massive structure with low contents of quartz and feldspar but high clay content. These evolutions of permeability have not been clearly clarified in current related literature.

7. Discussion

7.1. Enhancement of primary petroleum expulsion induced by generation of a permeable pore network in the low-mature stage

Initially, the decomposition of OM creates new pore spaces, which successively promotes the primary expulsion of liquid and gas products during the early oil stage or the beginning of oil window stage (Li et al., 2018; Wang et al., 2022; Liu et al., 2023a) (Figs. 13–19). At this stage (Ro < 0.8 %), large quantity of tiny cellular organic voids generated, and the small porosity increment is dominated by pores with radii 10 and 100 nm, followed by pores with radii of 100 nm–1000 nm (Figs. 11 and 13 F). This variation is consistent with the increase of mesopore from original state to pyrolysis temperature of 300 °C in the study of Liu et al. (2023b). However, this flow pathway increases have limited contribution to the fluid flow regarding the nanometer confinement effect, resulting in small permeability increment less than 0.0005 D, which can also be confirmed by the variation trend of total porosity from low mature to the beginning of mature stage observed by Wang et al. (2022) in the naturally matured shale samples (Figs. 11, 12 and 14 A–C, and Fig. 19 E). The small interdependent solid and space changes promote

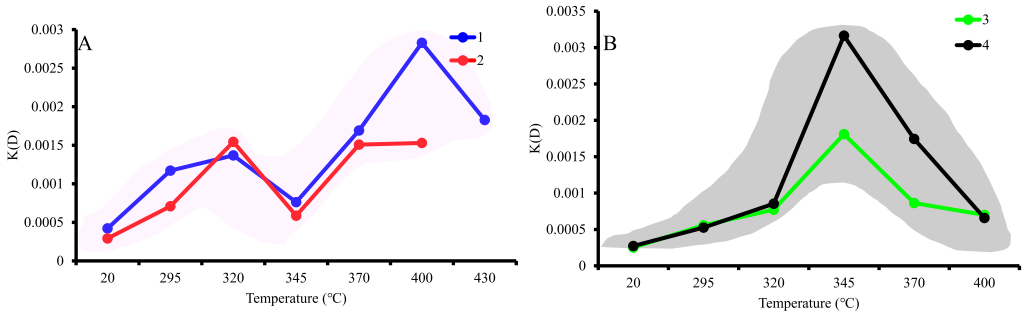

Fig. 12. The permeability evolution of the four samples during the thermal maturation (i.e. A. sample 1 and sample 2, B. sample 3 and sample 4).

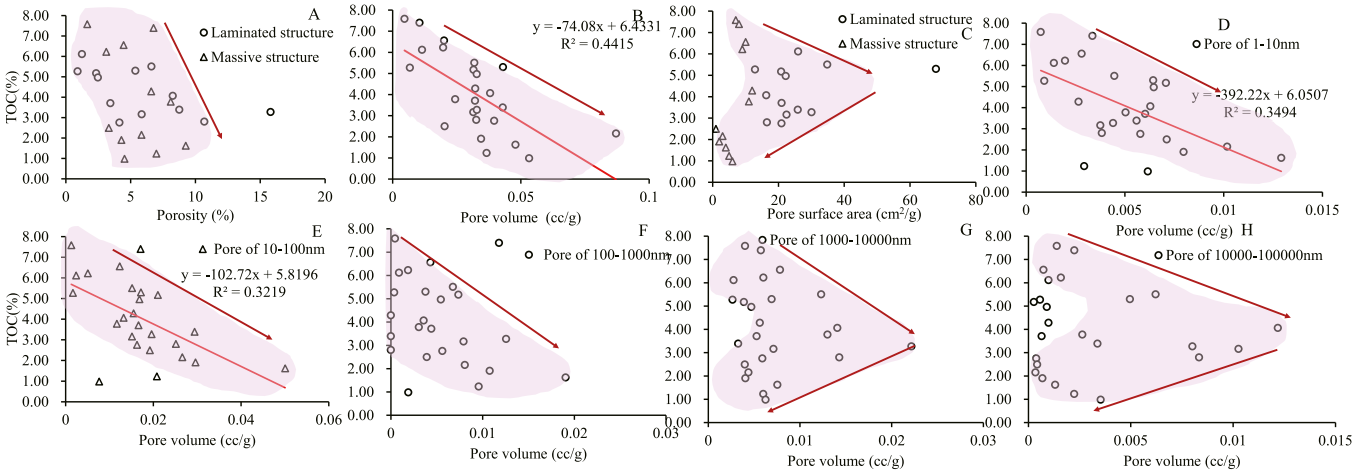

Fig. 13. The relations between the TOC and the petrophysical parameters during the thermal evolution (A. porosity, B. total pore volume, C. pore surface area, D. pore volume of pore of 1–10 nm, E. pore volume of pore of 10–100 nm, F. pore volume of pore of 100–1000 nm, G. pore volume of pore of 1000–10000 nm, and H. pore volume of pore of 10000–100000 nm).

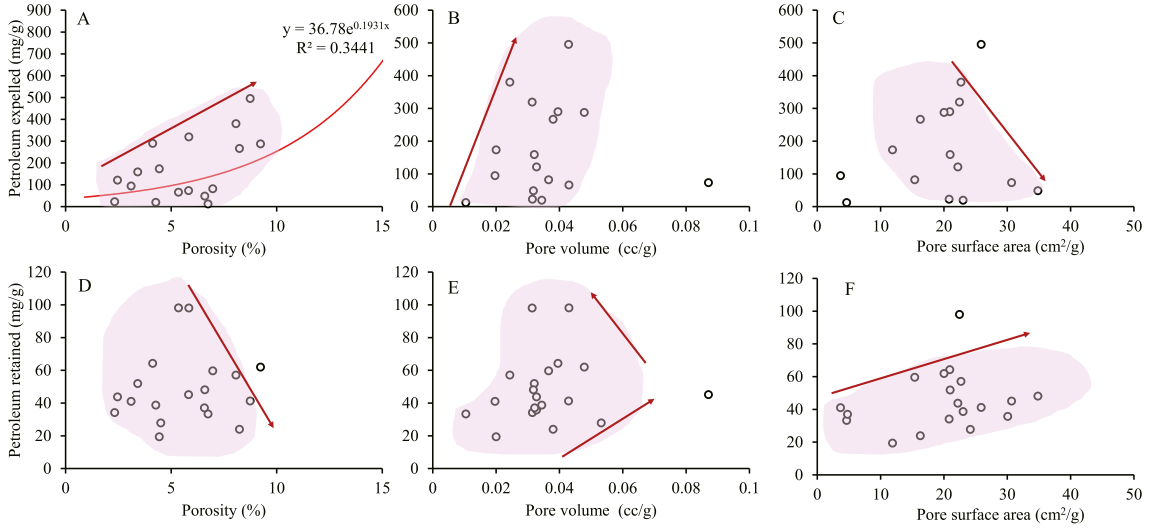

Fig. 14. The correlations between the quantity of the petroleum expelled and the petrophysical parameters during the thermal evolution (A. porosity, B. total pore volume, and C. pore surface area) and those between the quantity of the petroleum retained and the petrophysical parameters (D. porosity, E. total pore volume, and F. pore surface area).

the expulsion of the gas and liquid products, where the ratio of the expulsion petroleum to that retained rising from approximately 1 to >2 from 295 °C to 320 °C, much higher than the ratio of produced immiscible oil to bitumen in the rock during the similar stage of the Green River shale that reported by Ruble et al. (2001) (Figs. 5, 6 and 14 A–C, and Fig. 19 B).

7.2. Complex evolution of solid matrix, void space, and fluid phases in the mature to highly mature stages

Porosity growth as well as permeability increment slow down with increasing temperature and even a reversal presents at the end of low mature stage or beginning of mature stage (Figs. 6 and 12). This is because of the rising content of heavy compounds in the retained liquid petroleum in shale matrix with accelerating decomposition of OM, of which the rising asphaltene retention aggravates the pore blockage (Fig. 14 D and E, M-P, Fig. 16 A–H). The heavy liquids with high asphaltene content fill the fluid flow pathways, e.g. pores with width of 10 nm–10000 nm, decreasing the porosity and permeability and hindering the asphaltene expulsion in turn (Fig. 15 E–H). This pore blockage effect has been confirmed by the evident volume increment of micropores after the bitumen has been extracted from the North American shale samples in the study of Valenza et al. (2013). With the temperature rising to 345 °C (Ro 1.0 %), the massive gas and liquid petroleum generated from maximum thermal decomposition and cracking brings considerable volumetric expansion, resulting in the growths of microfractures of 1000 nm–10000 nm and 10000 nm–100000 nm and volume expansion of meso- and macropores (Fig. 14A–E, Fig. 18 E–H). This strongly promotes the second-time permeability and porosity increments, which bring a maximum liquid petroleum expulsion in turn, consistent with the immiscible oil production rate of Xiamaling shale at the Ro of 1.0 %–1.5 % that conducted by Li et al. (2018) and can be confirmed by the little differences between the pore volume of micropores before and after bitumen extraction at the Ro of 1.5 %–2.0 % reported in Valenza et al. (2013) (Figs. 5, 6, 11–17). The significant wideness of the fluid flow channels enhances the mobility of the heavy aromatic hydrocarbon and asphaltene, which has also been revealed in the pyrolysis of Green River shale at 325 °C–350 °C

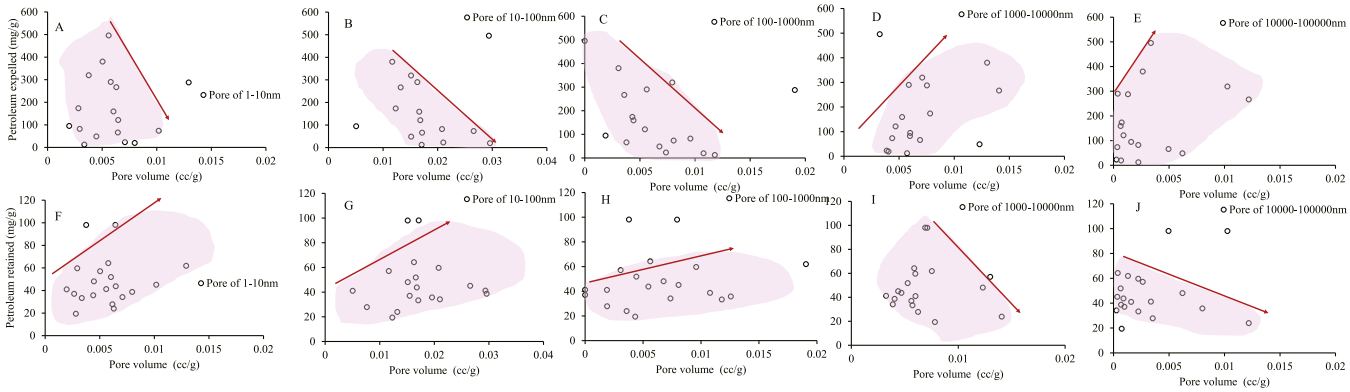

Fig. 15. The correlations between the quantity of the petroleum expelled and the pore volume of certain-sized pores during thermal maturation (A. pore volume of pore of 1–10 nm, B. pore volume of pore of 10–100 nm, C. pore volume of pore of 100–1000 nm, D. pore volume of pore of 1000–10000 nm, and E. pore volume of pore of 10000–100000 nm) and those between the quantity of the petroleum retained and the pore volume of certain-sized pores (F. pore volume of pore of 1–10 nm, G. pore volume of pore of 10–100 nm, H. pore volume of pore of 100–1000 nm, I. Pore volume of pore of 1000–10000 nm, and J. pore volume of pore of 10000–100000 nm).

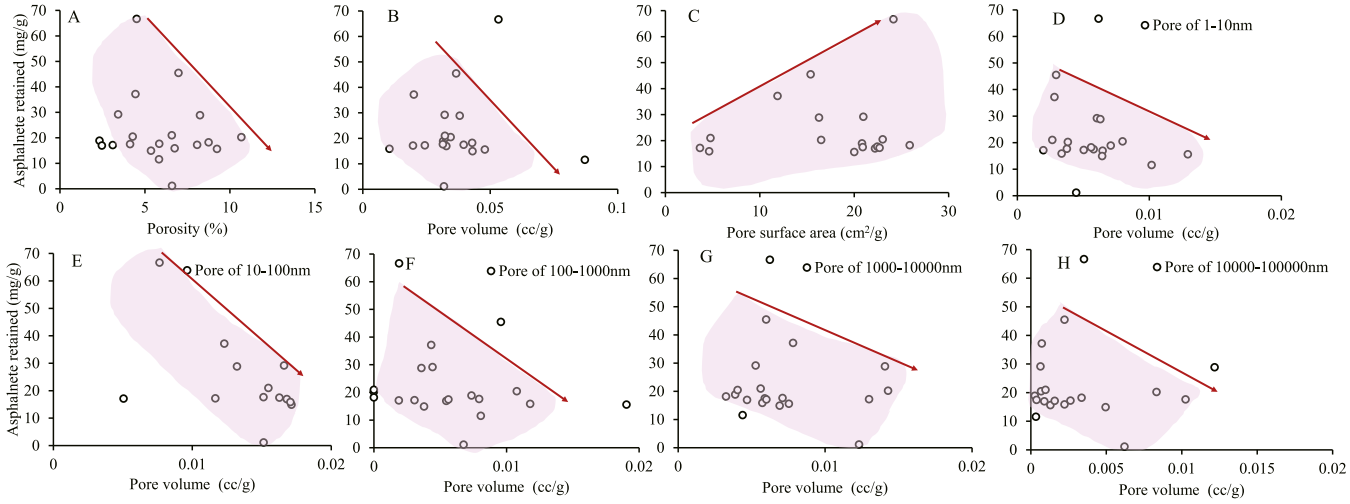

Fig. 16. The correlations between the quantity of the asphaltene retained and the petrophysical properties during the thermal evolution (A. porosity, B. total pore volume, C. pore surface area, D. pore volume of pore of 1–10 nm, E. pore volume of pore of 10–100 nm, F. pore volume of pore of 100–1000 nm, G. pore volume of pore of 1000–10000 nm, and H. pore volume of pore of 10000–100000 nm).

(Tiwari et al., 2013; Saif et al., 2016) (Figs. 4 and 17 E–H). From low mature to mature stage, the shales with different laminations share similar simultaneous geochemical and petrophysical evolutions with exception for the changes in pore size range and expulsion quantity and its components. The pore space changes concentrate in 10 nm–1000 nm and lower petroleum quantity with higher heavy component is expelled in the massive shale (Figs. 13–19).

7.3. Evolution patterns in shales with different textures at high maturity

The evolution pattern differs in the shales with different textures with maturation rising to high mature stages (370°C–400 °C, Ro 1.2 %–2.0 %). For the laminated one, the expansion of the pore space continues as the continuous OM decomposition and discharge of the products, besides, the orientated rigid crystals provide extra grain support to pore spaces, leading to a continuous porosity and permeability increase (Figs. 5, 6, 11–19). The sharp volume increment of mesopore and macropore in the postmature stage of the lacustrine Qingshankou shale in the study of Liu et al. (2023a, 2023b), the evident volume increment of pores > 1000 nm of Wangqing oil shale at pyrolysis temperature of 430 °C in the study of Lei et al. (2021) and the massive macropore and fracture generation at 425 °C reported by Tiwari et al. (2013) strongly support the observed results. This improvement promotes the fluidity of the heavy aromatic hydrocarbon and asphaltene (Fig. 16 E–H, Fig. 17 E–H). On the other hand, the product expulsion promotion accelerates the chemical reaction rate of OM regarding the reaction equilibrium, evidenced by the greater TOC reduction in thin lamination shale (Figs. 3, 4, 15 and 19), and can also be supported by the reduction trends of the Green River shale (Ruble et al., 2001, 2003; Curry, 2003).

The porosity and permeability variation trend reverses in the massive shales, which experiences an evident second-time reduction, where the contents of pores of 100–1000 nm and 1000–10000 nm decrease more than 30 % or even up to 50 % (Figs. 6 and 11 C–D, Figs. 12 and 19), which has been rarely observed in previous publications. There are two reasons for the reverse, one of which is the hysteretic generation of the heavy asphaltene and the other is collapse of the created pore spaces and microfractures owing to the absence of grain support from the rigid grains of quartz and feldspar (Fig. 4 C and D, Table 1). Pore collapse and fracture healing lead to a higher asphaltene retention of approximately 8 % (Fig. 5 G, H, J, K, Fig. 13 G, H, and Fig. 19 E, F) than the laminated shale. The porosity evolution is complicated in the massive shales during this stage. The sample 4 with high TOC

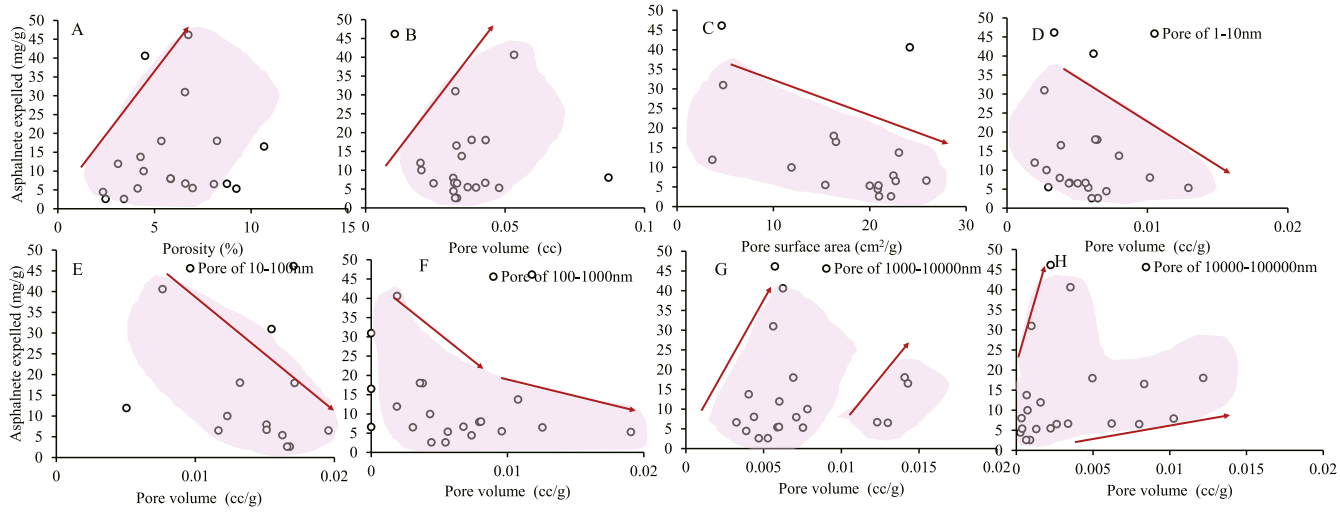

Fig. 17. The correlations between the quantity of the asphaltene expelled and the petrophysical parameters (A. porosity, B. total pore volume, C. pore surface area, D. pore volume of pore of 1–10 nm, E. pore volume of pore of 10–100 nm, F. pore volume of pore of 100–1000 nm, G. pore volume of pore of 1000–10000 nm, and H. pore volume of pore of 10000–100000 nm).

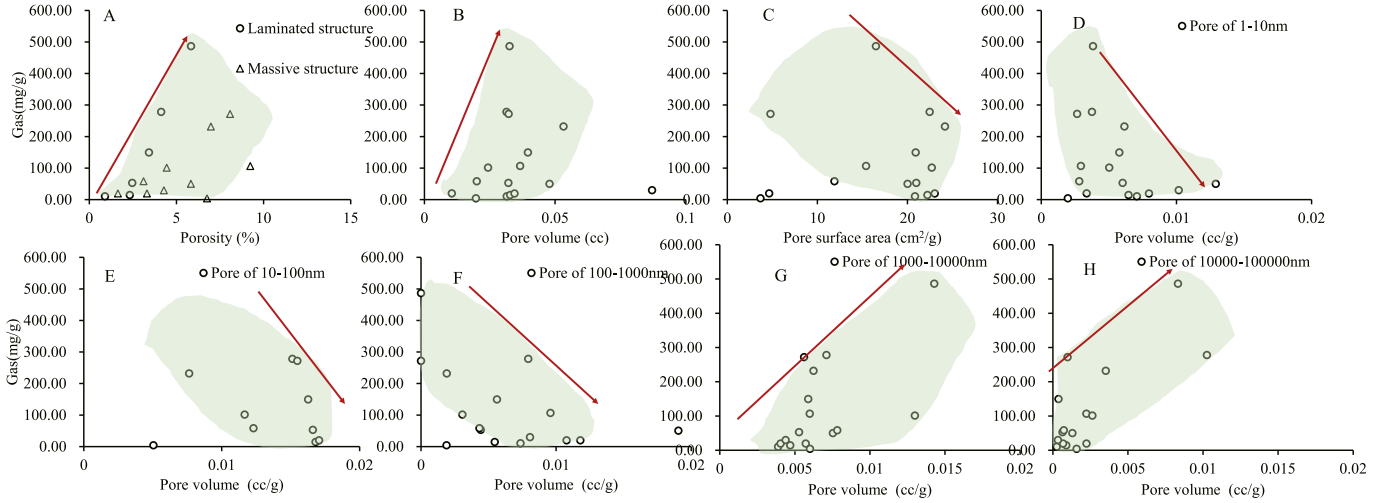

Fig. 18. The correlations between expelled gas quantity and the petrophysical properties during the thermal evolution (A. porosity, B. total pore volume, C. pore surface area, D. pore volume of pore of 1–10 nm, E. pore volume of pore of 10–100 nm, F. pore volume of pore of 100–1000 nm, G. pore volume of pore of 1000–10000 nm, and H. pore volume of pore of 10000–100000 nm).

experiences a second-time fracture opening at 370°C–400 °C due to the hysteretic OM decomposition, while the one with low TOC shows a gradually descending trend (Figs. 6, 12, 13 A and Fig. 17 A).

7.4. Simultaneous evolution of petrophysical and geochemical properties in organic-rich lacustrine shales with different textures

We can picture that the petrophysical and geochemical properties evolve interdependently during the thermal maturation of the organic-rich lacustrine shale (Fig. 20). The rule can be described as that the thermal OM decomposition comes first and results in the generation of organic micro- and meso-pores, where the porosity and permeability increment follow, and this increment promotes the expulsion of the liquid and gas products in low-mature stage (Fig. 20 A–C, G-I). The massive generation of liquid petroleum with higher asphaltene and aromatic hydrocarbon blocks the pore spaces at the beginning of the mature stage, leading to the petrophysical property descends and successive heavy component retention (Fig. 18 D–J). The acceleration of OM decomposition brings excessive volume expansion, resulting in the generation of the macropores and fractures that strongly promote the porosity and permeability increases and arise the expulsion efficiency in turn in the later mature stage (Fig. 20 E–K). The simultaneous variation during the low mature to the late state of mature stage can also be evidenced by the combined analysis of previous publications in the Green River shale and Qingshankou shale in Songliao Basin (Ruble et al., 2001; Lewan and Ruble, 2002; Curry, 2003; Chen and Xiao, 2014; Lei et al., 2021; Wang et al., 2022; Liu et al., 2023a, 2023b; Hazra et al., 2024). The evolution complicates from mature to high-mature stage owing to the different orientated minerals in shales with different laminations. The laminated shale is characterized by a second-time porosity and permeability increases, while the massive one is on the contrary. Therefore, more asphaltene is retained in the massive shale.

7.5. Implications for the subsurface in-situ retorting and combustion of lacustrine shale

The variation rules indicated from the integrated experimental results suggest that the best retorting temperature of lacustrine organic

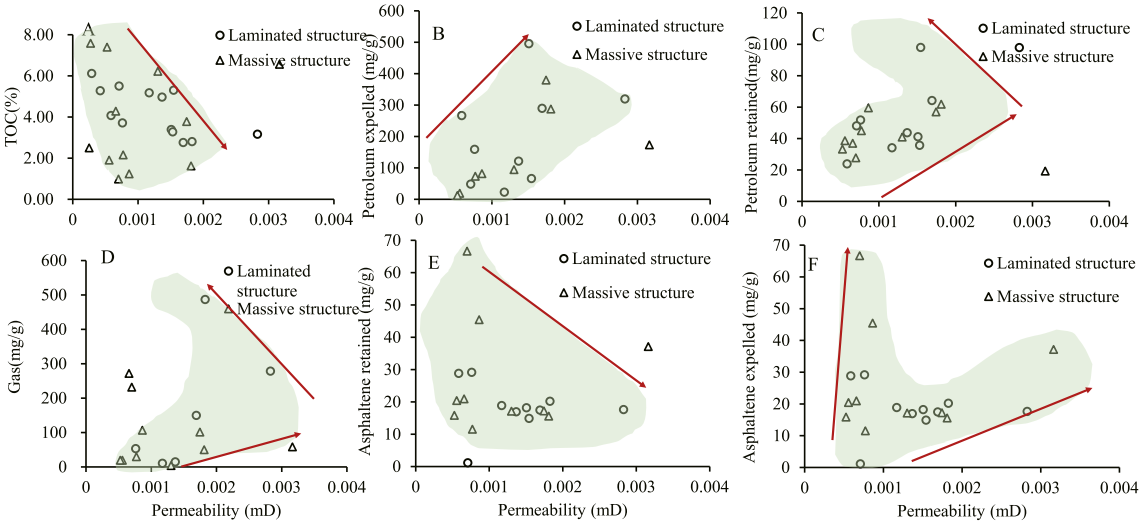

Fig. 19. The correlations between permeability and the geochemical properties during the thermal maturation (A. TOC, B. petroleum expelled, C. petroleum retained, D. gas expelled, E. asphaltene retained, and F. asphaltene expelled).

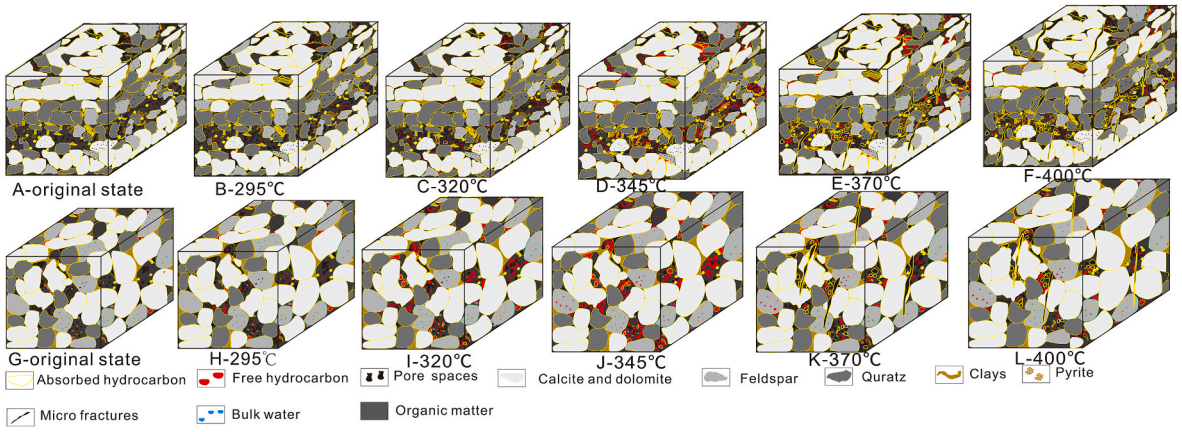

Fig. 20. Sketch illustrating the conceptual evolution patterns of the pore-space, rock matrix, and pore fluid distribution in fine-grained organic-rich sediments with different textures during the thermal maturation. A–G: laminated, I–M: unlaminated.

matter-rich shale in the field is between 370 °C and 400 °C. The massive liquid petroleum generation and accompanied significant fluid flow pathway enhancement indicate that more valuable liquid petroleum with relatively high saturated hydrocarbon expels naturally from the shale, which can significantly improve the development efficiency. Moreover, considering the effects of lamination, TOC, and thermal maturity on the hydrocarbon generation and changes in microstructure, the in-situ pyrolysis temperature selected in the heating program of filed retorting may vary in a shale horizon (Lei et al., 2021; Liu et al., 2023a; Hazra et al., 2023, 2024). The creation of micro- and mesopores of 10–100 nm in the low mature and in the early mature stage of lacustrine organic shale can be used for the sequestrating sites for CO_2, which can provide useful information for the strategy of the site selection of CO_2 sequestration in the shale formation (Hazra et al., 2022). It suggests that the low matured and early matured massive lacustrine shale is better targets. The creation and propagation of the microfractures in the late mature and high mature stage, significantly enhance the connectivity of the pore network and the shale oil recovery, provide useful insights for the formation and crack patterns of the thermal induced fractures and the project design in the thermally simulated shale horizon (Saif et al., 2016; Geng et al., 2017).

8. Conclusions

This work uncovers the simultaneous petrophysical and geochemical evolutions of the lacustrine organic matter-rich shale during the thermal maturation by integrating hydrous pyrolysis with a series of populated geochemical and petrophysical measurements and improved shale porosity and permeability evaluation methods. The main findings can be drawn as follow.

(1) The key finding lies in the interdependent evolutions of porosity, permeability, organic matter, and pyrolyzed petroleum products originated from the coupled interactions from the solid, void space, and liquid phases.
(2) The interaction starts with OM decomposition and liquid hydrocarbon generation, accompanied by micro- and meso-pores generation in low mature stage (295°C–320 °C and Ro 0.8 %–1.0 %). The eightfold increase of tiny organic spaces exerts slight enhancement on the porosity and permeability, which promotes the primary liquid petroleum expulsion in turn. With the continuous decomposition to the end of low mature stage (320 °C), the massive generation of liquid petroleum with heavy components inhibits the petroleum expulsion due to the blockage

of flow pathways, slowing down or reversing the porosity and permeability variation trend.

(3) The porosity and permeability increment are augmented by the evident expansion and generation of the mesopores and macropores with pore radii >100 nm during mature stage, which simultaneously promotes the petroleum expulsion and OM decomposition in turn. The thermal decomposition reaches its peak during 345 °C–370 °C, which brings quantity macropores and fractures with width >10000 nm, where a second-time porosity and permeability increases happen successively. Mutual promotions between petrophysical and geochemical property evolutions happen in this process.

(4) Two different patterns occur from the end of mature to high mature stage in shales with laminated and massive textures. The developed rigid grains with certain orientation serve as support skeleton to the pores and fractures generated. This support is weakened in the massive shales with lower rigid grain content, where a pore space collapse or fracture healing happens when the self-supports of OM solids disappear in high mature stage. Hence, the laminated shale exhibits a continuous increasing petrophysical trend, the massive one is on the contrary. Successively, the asphaltene content expelled is greater and content retained is much lower in laminated shale. The decrease in the petrophysical properties also results in a hysteresis in the OM decomposition in massive shales in turn, indicating IM lamina is advantageous for the hydrocarbon generation and expulsion.

Our findings indicate that the best in-situ retorting temperature of low-mature fine-grained organic matter-rich shale is 345 °C–370 °C regarding of the generation and expulsion quantity of light hydrocarbon and favorable flow paths, especially in laminated shale. The hysteresis of liquid petroleum generation and expulsion in massive shale suggests a petrophysical property improvement at 400 °C. The low-matured shale with high micropore content can serve as potential sequestrating sites for CO_2. Theoretically, differences in the geochemical evolution of shale with different textures can serve as a compliment to the Tissot model and current hydrocarbon generation threshold theory, and these results also reminds the scientist who are working on the porosity and permeability evaluation to emphasize the effects from the matrix texture, maturation, and liquid product.

CRediT authorship contribution statement

Juncheng Qiao: Writing – original draft, Resources, Investigation, Conceptualization, Writing – review & editing, Supervision, Methodology, Funding acquisition. **Jianhui Zeng:** Resources, Methodology, Supervision, Project administration. **Guangqing Yang:** Investigation, Data curation, Software, Formal analysis. **Zhe Cao:** Validation, Formal analysis, Methodology. **Yazhou Liu:** Visualization, Software. **XiuJuan Zhang:** Visualization, Validation.

Declaration of competing interest

The authors declare that they have no known competing financial interests or personal relationships that could have appeared to influence the work reported in this paper.

Acknowledgement

This study is supported by the National Natural Science Foundation of China (No. 42302144) and Foundation of China University of Petroleum Beijing (No. 2462023BJRC012). It is a team work completed with good cooperation of all of the authors. We sincerely appreciate Dr. Bernad Krooss for helping us to improve the quaility and readability of the work. We also sincerely appreciate all anonymous reviewers and the handling editor for their comments and suggestions.

Data availability

Data will be made available on request.

References

Aguilera, R., 2014. Flow units: from conventional to tight-gas to shale-gas to tight-oil to shale-oil reservoirs. SPE Reserv. Eval. Eng. 17 (2), 190–208.
Amrani, A., Lewan, M., Aizenshtat, Z., 2005. Stable sulfur isotope partitioning during simulated petroleum formation as determined by hydrous pyrolysis of Ghareb Limestone, Israel. Geochim. Cosmochim. Ac. 69, 5317–5331.
Ardakani, O.H., Sanei, H., Ghanizadeh, A., Lavoie, D., Chen, Z., Clarkson, C.R., 2018. Do all fractions of organic matter contribute equally in shale porosity? A case study from Upper Ordovician Utica Shale, southern Quebec, Canada. Mar. Petrol. Geol. 92, 794–808.
Arif, M., Mahmoud, M., Zhang, Y., Iglauer, S., 2021. X-ray tomography imaging of shale microstructures: a review in the context of multiscale correlative imaging. Int. J. Coal Geol. 233, 1–19, 103641.
Bahadur, J., Melnichenko, Y., Mastalerz, M., Furmann, A., Clarkson, C.R., 2014. Hierarchical pore morphology of cretaceous shale: a small-angle neutron scattering and ultrasmall-angle neutron scattering study. Energy Fuel. 28 (10), 6336–6344.
Behar, F., Vandenbroucke, M., Tang, Y., Marquis, F., Espitalie, J., 1997. Thermal cracking of kerogen in open and closed systems: determination of kinetic parameters and stoichiometric coefficients for oil and gas generation. Org. Geochem. 26 (5–6), 321–339.
Behar, F., Roy, S., Jarvie, D., 2010. Artificial maturation of a Type I kerogen in closed system: mass balance and kinetic modelling. Org. Geochem. 41, 1235–1247.
Bennett, R.H., 1991. Microstructure of fine-grained Sediments: from Mud to Shale. Springer Science & Business Media, New York.
Berner, U., Faber, E., 1996. Empirical carbon isotope/maturity relationships for gases from algal kerogens and terrigenous organic matter, based on dry, open-system pyrolysis. Org. Geochem. 24 (10–11), 947–955.
Beskok, A., Karniadakis, G.E., 1999. Report: a model for flows in channels, pipes, and ducts at micro and nano scales. Microscale Therm. Eng. 3 (1), 43–77.
Borjigin, T., Longfei, L., Lingjie, Y., Zhang, W., Anyang, P., Baojian, S., et al., 2021. Formation, preservation and connectivity control of organic pores in shale. Petrol. Explor. Dev. 48 (4), 798–812.
Bustin, R.M., Bustin, A.M., Cui, A., Ross, D., Pathi, V.M., 2008. Impact of shale properties on pore structure and storage characteristics. In: SPE Shale Gas Production Conference in Fort Worth, Texas.
Cao, J., Zhang, Y., Hu, W., Yao, S., Wang, X., Zhang, Y., et al., 2005. The Permian hybrid petroleum system in the northwest margin of the Junggar Basin, northwest China. Mar. Petrol. Geol. 22 (3), 331–349.
Cao, Z., Liu, G., Kong, Y., Wang, C., Niu, Z., Zhang, J., et al., 2016. Lacustrine tight oil accumulation characteristics: permian Lucaogou Formation in Jimusaer sag, Junggar Basin. Int. J. Coal Geol. 153, 37–51.
Carroll, A.R., Yunhai, L., Graham, S.A., Xuchang, X., Hendrix, M.S., Jinchi, C., et al., 1990. Junggar basin, northwest China: trapped late Paleozoic ocean. Tectonophysics 181 (1–4), 1–14.
Carvajal-Ortiz, H., Gentzis, T., 2015. Critical considerations when assessing hydrocarbon plays using Rock-Eval pyrolysis and organic petrology data: data quality revisited. Inter. J. Coal. Geol. 152, 113–122.
Chalmers, G.R., Bustin, R.M., Power, I.M., 2012. Characterization of gas shale pore systems by porosimetry, pycnometry, surface area, and field emission scanning electron microscopy/transmission electron microscopy image analyses: examples from the Barnett, Woodford, Haynesville, Marcellus, and Doig units. AAPG Bull. 96 (6), 1099–1119.
Chang, J., Fan, X., Jiang, Z., Wang, X., Chen, L., Li, J., et al., 2022. Differential impact of clay minerals and organic matter on pore structure and its fractal characteristics of marine and continental shales in China. Appl. Clay Sci. 216, 1–13, 106334.
Chen, J., Xiao, X., 2014. Evolution of nanoporosity in organic-rich shales during thermal maturation. Fuel 129, 173–181.
Clarkson, C.R., Freeman, M., He, L., Agamalian, M., Melnichenko, Y., Mastalerz, M., et al., 2012. Characterization of tight gas reservoir pore structure using USANS/SANS and gas adsorption analysis. Fuel 95 (3), 71–85.
Clarkson, C.R., Solano, N., Bustin, R.M., Bustin, A., Chalmers, G., He, L., et al., 2013. Pore structure characterization of North American shale gas reservoirs using USANS/SANS, gas adsorption, and mercury intrusion. Fuel 103, 606–616.
Clarkson, C., Haghshenas, B., Ghanizadeh, A., Qanbari, F., Williams-Kovacs, J., Riazi, N., et al., 2016. Nanopores to megafractures: current challenges and methods for shale gas reservoir and hydraulic fracture characterization. J. Nat. Gas Sci. Eng. 31, 612–657.
Cnudde, V., Boone, M.N., 2013. High-resolution X-ray computed tomography in geosciences: a review of the current technology and applications. Earth Sci. Rev. 123, 1–17.
Crombez, V., Baudin, F., Rohais, S., Riquier, L., Euzen, T., Pauthier, S., et al., 2017. Basin scale distribution of organic matter in marine fine-grained sedimentary rocks: insight from sequence stratigraphy and multi-proxies analysis in the Montney and Doig formations. Mar. Petrol. Geol. 83, 382–401.
Curry, D., 2003. New insights on the Green River petroleum system in the Uinta basin from hydrous pyrolysis experiments: discussion. AAPG Bull. 87, 1531–1534.
Curry, K.J., Bennett, R.H., Mayer, L.M., Curry, A., Abril, M., Biesiot, P.M., et al., 2007. Direct visualization of clay microfabric signatures driving organic matter

preservation in fine-grained sediment. Geochimi. Cosmochimi. Ac. 71 (7), 1709–1720.
Curtis, J.B., 2002. Fractured shale-gas systems. AAPG Bull. 86 (11), 1921–1938.
Curtis, M.E., 2010. Structural characterization of gas shales on the micro-and nano-scales. In: Canadian Unconventional Resources and International Petroleum Conference. SPE.
Curtis, M.E., Cardott, B.J., Sondergeld, C.H., Rai, C.S., 2012a. The development of organic porosity in the Woodford Shale related to thermal maturity. In: SPE Annual Technical Conference and Exhibition, San Antonio, Texas.
Curtis, M.E., Sondergeld, C.H., Ambrose, R.J., Rai, C.S., 2012b. Microstructural investigation of gas shales in two and three dimensions using nanometer-scale resolution imagingMicrostructure of Gas Shales. AAPG Bull. 96 (4), 665–677.
Darabi, H., Ettehad, A., Javadpour, F., Sepehrnoori, K., 2012. Gas flow in ultra-tight shale strata. J. Fluid Mech. 710, 641–658.
Davudov, D., Moghanloo, R.G., 2018. Impact of pore compressibility and connectivity loss on shale permeability. Int. J. Coal Geol. 187, 98–113.
Ding, X., Qu, J., Imin, A., Zha, M., Su, Y., Jiang, Z., et al., 2019. Organic Matter Origin and Accumulation in Tuffaceous Shale of the Lower Permian Lucaogou Formation, Jimsar Sag. J. Petrol. Sci. Eng. 179, 696–706.
Dyni, J.R., 2003. Geology and resources of some world oil-shale deposits. Oil Shale 20 (3), 193–252.
EIA, 2015. World Shale Resource Assessments. Energy Information Administration, Washington, DC.
Geng, Y., Liang, W., Liu, J., Cao, M., Kang, Z., 2017. Evolution of pore and fracture structure of oil shale under high temperature and high pressure. Energy Fuel. 31, 10404–10413.
Glorioso, J.C., Rattia, A., 2012. Unconventional reservoirs: basic petrophysical concepts for shale gas. In: SPE/EAGE European Unconventional Resources Conference and Exhibition, Vienna, Austria.
Gou, Q., Xu, S., Hao, F., Yang, F., Zhang, B., Shu, Z., et al., 2019. Full-scale pores and micro-fractures characterization using FE-SEM, gas adsorption, nano-CT and micro-CT: a case study of the Silurian Longmaxi Formation shale in the Fuling area, Sichuan Basin, China. Fuel 253, 167–179.
Gupta, N., Fathi, E., Belyadi, F., 2018. Effects of nano-pore wall confinements on rarefied gas dynamics in organic rich shale reservoirs. Fuel 220, 120–129.
Hackley, P.C., Fishman, N., Wu, T., Baugher, G., 2016. Organic petrology and geochemistry of mudrocks from the lacustrine Lucaogou Formation, Santanghu Basin, northwest China: application to lake basin evolution. Int. J. Coal Geol. 168, 20–34.
Han, H., Guo, C., Zhong, N., Pang, P., Gao, Y., 2020. A study on fractal characteristics of lacustrine shales of Qingshankou Formation in the Songliao Basin, northeast China using nitrogen adsorption and mercury injection methods. J. Petrol. Sci. Eng. 193, 1–14, 107378.
Hao, F., Zou, H., 2013. Cause of shale gas geochemical anomalies and mechanisms for gas enrichment and depletion in high-maturity shales. Mar. Petrol. Geol. 44, 1–12.
Hazra, B., Dutta, S., Kumar, S., 2017. TOC calculation of organic matter rich sediments using Rock-Eval pyrolysis: critical consideration and insights. Int. J. Coal Geol. 169, 106–115.
Hazra, B., Karacan, C.Ö., Tiwari, D.M., Singh, P.K., Singh, A.K., 2019. Insights from Rock-Eval analysis on the influence of sample weight on hydrocarbon generation from Lower Permian organic matter rich rocks, West Bokaro basin, India. Mar. Petrol. Geol. 106, 160–170.
Hazra, B., Vishal, V., SethiC, Chandra D., 2022. Impact of supercritical CO_2 on shale reservoirs and its implication for CO_2 sequestration. Energy Fuel. 36, 9882–9903.
Hazra, B., Chandra, D., Lahiri, S., Vishal, V., Sethi, C., Pandey, J.K., 2023. Pore evolution during combustion of distinct thermally mature shales: insights into potential in situ conversion. Energy Fuel. 37, 13898–13911.
Hazra, B., Chandra, D., Vishal, V., Ostadhassan, M., Sethi, C., Saikia, B., et al., 2024. Experimental study on pore structure evolution of thermally treated shales: implications for CO2 storage in underground thermally treated shale horizons. Inter. J. Coal Sci. Techno. 11 (61), 1–21.
Hedges, J.I., Keil, R.G., 1995. Sedimentary organic matter preservation: an assessment and speculative synthesis. Mar. Chem. 49 (2–3), 81–115.
Huizinga, B., Aizenshtat, Z., Peters, K., 1988. Programmed pyrolysis-gas chromatography of artificially matured Green River kerogen. Energy Fuel. 2, 74–81.
Jarvie, D.M., Hill, R.J., Ruble, T.E., Pollastro, R.M., 2007. Unconventional shale-gas systems: the Mississippian Barnett Shale of north-central Texas as one model for thermogenic shale-gas assessment. AAPG Bull. 91 (4), 475–499.
Javadpour, F., 2009. Nanopores and apparent permeability of gas flow in mudrocks (shales and siltstone). J. Canadian Petrol. Tech. 48 (8), 16–21.
Kuila, U., Prasad, M., 2013. Specific surface area and pore-size distribution in clays and shales. Geophys. Prospect. 61 (2), 341–362.
Kuila, U., McCarty, D.K., Derkowski, A., Fischer, T.B., Topór, T., Prasad, M., 2014. Nano-scale texture and porosity of organic matter and clay minerals in organic-rich mudrocks. Fuel 135, 359–373.
Lei, J., Pan, B., Guo, Y., Fan, Y., Xue, L., Deng, S., et al., 2021. A comprehensive analysis of the pyrolysis effects on oil shale pore structures at multiscale using different measurement methods. Energy 227, 1–15, 120359.
Lewan, M., 1994. Assessing natural oil expulsion from source rocks by laboratory pyrolysis. In: Magoon, L.B., Dow, W.G. (Eds.), The Petroleum System—From Source to Trap, vol. 60. American Association of Petroleum Geologists Memoir, pp. 201–210.
Lewan, M., Ruble, T., 2002. Comparison of petroleum generation kinetics by isothermal hydrous and nonisothermal open-system pyrolysis. Org. Geochem. 33, 1457–1475.
Lewan, M., Kotarba, M., Curtis, J., Więcław, D., Kosakowski, P., 2006. Oil-generation kinetics for organic facies with Type-II and-IIs kerogen in the Menilite Shales of the Polish Carpathians. Geochim. Cosmochim. Ac. 70, 3351–3368.
Li, J., Yin, J., Zhang, Y., Lu, S., Wang, W., Li, J., et al., 2015. A comparison of experimental methods for describing shale pore features—A case study in the Bohai Bay Basin of eastern China. Inter. J. Coal. Geol. 152, 39–49.
Li, J., Ma, W., Wang, Y.F., Wang, D.L., Xie, Z.Y., Li, Z.S., et al., 2018. Modeling of the whole hydrocarbon-generating process of sapropelic source rock. Petrol. Explor. Dev. 45, 461–471.
Li, X., Cai, J., Liu, H., Zhu, X., Li, Z., Liu, J., 2020. Characterization of shale pore structure by successive pretreatments and its significance. Fuel 269, 1–15, 117412.
Liu, Y., Yao, Y., Liu, D., Zheng, S., Sun, G., Chang, Y., 2018. Shale pore size classification: an NMR fluid typing method. Mar. Petrol. Geol. 96, 591–601.
Liu, H., Zhang, S., Song, G., Xuejun, W., Teng, J., Wang, M., et al., 2019. Effect of shale diagenesis on pores and storage capacity in the Paleogene Shahejie Formation, Dongying Depression, Bohai Bay Basin, east China. Mar. Petrol. Geol. 103, 738–752.
Liu, B., Mohammadi, M.-R., Ma, Z., Bai, L., Wang, L., Xu, Y., et al., 2023a. Pore structure evolution of Qingshankou shale (kerogen type I) during artificial maturation via hydrous and anhydrous pyrolysis: experimental study and intelligent modeling. Energy 282, 1–19, 128359.
Liu, B., Mohammadi, M., Ma, Z., Bai, L., Wang, L., Xu, Y., Ostadhassan, M., et al., 2023b. Evolution of porosity in kerogen type I during hydrous and anhydrous pyrolysis: experimental study, mechanistic understanding, and model development. Fuel 338, 1–21, 127149.
Löhr, S., Baruch, E., Hall, P., Kennedy, M., 2015. Is organic pore development in gas shales influenced by the primary porosity and structure of thermally immature organic matter? Org. Geochem. 87, 119–132.
Loucks, R.G., Reed, R.M., Ruppel, S.C., Jarvie, D.M., 2009. Morphology, genesis, and distribution of nanometer-scale pores in siliceous mudstones of the Mississippian Barnett Shale. J. Sediment. Res. 79 (12), 848–861.
Ma, L., Taylor, K.G., Dowey, P.J., Courtois, L., Gholinia, A., Lee, P.D., 2017. Multi-scale 3D characterisation of porosity and organic matter in shales with variable TOC content and thermal maturity: examples from the Lublin and Baltic Basins, Poland and Lithuania. Int. J. Coal Geol. 180, 100–112.
Mastalerz, M., Schimmelmann, A., Drobniak, A., Chen, Y., 2013. Porosity of Devonian and Mississippian new Albany shale across a maturation gradient: insights from organic petrology, gas adsorption, and Mercury intrusion. AAPG Bull. 97 (10), 1621–1643.
Mayer, L.M., Schick, L.L., Hardy, K.R., Wagai, R., McCarthy, J., 2004. Organic matter in small mesopores in sediments and soils. Geochimi. Cosmochimi. Ac. 68 (19), 3863–3872.
Milliken, K.L., Day-Stirrat, R.J., 2013. Cementation in Mudrocks: Brief Review with Examples from Cratonic Basin Mudrocks, vol.103. AAPG Special Volumes, Memoir, pp. 133–150. Critical Assessment of Shale Resource Plays.
Mishra, S., Mendhe, V.A., Varma, A.K., Kamble, A.D., Sharma, S., Bannerjee, M., et al., 2018. Influence of organic and inorganic content on fractal dimensions of Barakar and Barren Measures shale gas reservoirs of Raniganj basin, India. J. Nat. Gas Sci. Eng. 49, 393–409.
Pang, H., Pang, X-q, Dong, L., Zhao, X., 2018. Factors impacting on oil retention in lacustrine shale: permian Lucaogou Formation in Jimusaer Depression, Junggar Basin. J. Petrol. Sci. Eng. 163, 79–90.
Pang, X., Wang, G., Kuang, L., Li, H., Zhao, Y., Li, D., et al., 2022. Insights into the pore structure and oil mobility in fine-grained sedimentary rocks: the Lucaogou Formation in Jimusar Sag, Junggar Basin, China. Mar. Petrol. Geol. 137, 1–19, 105492.
Pollastro, R.M., Cook, T.A., Roberts, L.N., Schenk, C.J., Lewan, M.D., Anna, L.O., et al., 2008. Assessment of Undiscovered Oil Resources in the Devonian-Mississippian Bakken Formation, Williston Basin Province, Montana and North Dakota. Geological Survey (US), 2008.
Potter, P.E., Maynard, J.B., Pryor, W.A., 2012. Sedimentology of Shale: Study Guide and Reference Source. Springer Science & Business Media, New York.
Qiao, J., Zeng, J., Jiang, S., Wang, Y., 2020a. Impacts of sedimentology and diagenesis on pore structure and reservoir quality in tight oil sandstone reservoirs: implications for macroscopic and microscopic heterogeneities. Mar. Petrol. Geol. 111, 279–300.
Qiao, J., Zeng, J., Jiang, S., Ma, Y., Feng, S., Xie, H., et al., 2020b. Role of pore structure in the percolation and storage capacities of deeply buried sandstone reservoirs: a case study of the Junggar Basin, China. Mar. Petrol. Geol. 113, 1–19, 104129.
Qiao, J., Zeng, J., Jiang, S., Yang, G., Zhang, Y., Feng, X., et al., 2022. Investigation on the unsteady-state two-phase fluid transport in the nano-pore system of natural tight porous media. J. Hydro. 607, 1–18, 127516.
Revil, A., Cathles Iii, L., 1999. Permeability of shaly sands. Water Resour. Res. 35 (3), 651–662.
Rickman, R., Mullen, M., Petre, E., Grieser, B., Kundert, D., 2008. A practical use of shale petrophysics for stimulation design optimization: all shale plays are not clones of the Barnett Shale. In: SPE Annual Technical Conference and Exhibition, Denver, Colorado.
Rosenberg, Y., Meshoulam, A., Said-Ahmad, W., Shawar, L., Dror, G., Reznik, I., et al., 2017. Study of thermal maturation processes of sulfur-rich source rock using compound specific sulfur isotope analysis. Org. Geochem. 112, 59–74.
Rosenberg, Y., Reznik, I., Vinegar, H., Feinstein, S., Bartov, Y., 2021. Comparing natural and artificial thermal maturation of a Type II-S source rock, Late Cretaceous, Israel. Mar. Petrol. Geol. 124, 1–14, 104773.
Ross, D.J., Bustin, R.M., 2009. The importance of shale composition and pore structure upon gas storage potential of shale gas reservoirs. Mar. Petrol. Geol. 26 (6), 916–927.
Ruble, T., Lewan, M., Philp, R., 2001. New insights on the Green River petroleum system in the Uinta basin from hydrous pyrolysis experiments. AAPG Bull. 85, 1333–1371.

Ruble, T., Lewan, M., Paul, P., 2003. New insights on the Green River petroleum system in the Uinta basin from hydrous-pyrolysis experiments: reply. AAPG Bull. 87, 1535–1541.
Rutherford, S., Do, D., 1997. Review of time lag permeation technique as a method for characterisation of porous media and membranes. Adsorption 3, 283–312.
Saif, T., Lin, Q., Singh, K., Bijeljic, B., Blunt, M., 2016. Dynamic imaging of oil shale pyrolysis using synchrotron X-ray microtomography. Geophys. Res. Lett. 43, 6799–6807.
Sakhaee-Pour, A., Bryant, S.L., 2012. Gas permeability of shale. SPE Reser. Eval. Eng. 15 (4), 401–409.
Schrodt, J.T., Ocampo, A., 1984. Variations in the pore structure of oil shales during retorting and combustion. Fuel 63 (11), 1523–1527.
Sigal, R.F., 2015. Pore-size distributions for organic-shale-reservoir rocks from nuclear-magnetic-resonance spectra combined with adsorption measurements. SPE J. 20 (4), 824–830.
Sing, K.S., 1985. Reporting physisorption data for gas/solid systems with special reference to the determination of surface area and porosity (recommendations 1984). Pure Appl. Chem. 57 (4), 603–619.
Singh, H., Javadpour, F., Ettehadtavakkol, A., Darabi, H., 2014. Nonempirical apparent permeability of shale. SPE Reser. Eval. Eng. 17 (3), 414–424.
Smith, J., 1971. The dynamics of shale compaction and evolution of pore-fluid pressures. J. Int. Ass. Math. Geol. 3, 239–263.
Sondergeld, C.H., Newsham, K.E., Comisky, J.T., Rice, M.C., Rai, C.S., 2010. Petrophysical considerations in evaluating and producing shale gas resources. In: SPE Unconventional Resources Conference/Gas Technology Symposium, Pittsburgh, Pennsylvania.
Song, D., Tuo, J., Wu, C., Zhang, M., Su, L., 2020. Comparison of pore evolution for a Mesoproterozoic marine shale and a Triassic terrestrial mudstone during artificial maturation experiments. J. Nat. Gas Sci. Eng. 75, 1–16, 103153.
Tang, X., Jiang, Z., Jiang, S., Wang, P., Xiang, C., 2016. Effect of organic matter and maturity on pore size distribution and gas storage capacity in high-mature to post-mature shales. Energy Fuel. 30 (11), 8985–8996.
Thommes, M., Kaneko, K., Neimark, A.V., Olivier, J.P., Rodriguez-Reinoso, F., Rouquerol, J., et al., 2015. Physisorption of gases, with special reference to the evaluation of surface area and pore size distribution (IUPAC Technical Report). Pure Appl. Chem. 87 (9–10), 1051–1069.
Tiwari, P., Deo, M., Lin, C., Miller, J., 2013. Characterization of oil shale pore structure before and after pyrolysis by using X-ray micro CT. Fuel 107, 547–554.
Valenza, J.J., Drenzek, N., Marques, F., Pagels, M., Mastalerz, M., 2013. Geochemical controls on shale microstructure. Geology 41 (5), 611–614.
Vandenbroucke, M., Largeau, C., 2007. Kerogen origin, evolution and structure. Org. Geochem. 38, 719–833.
Wang, F.P., Reed, R.M., John, A., Katherine, G., 2009. Pore networks and fluid flow in gas shales. In: SPE Annual Technical Conference and Exhibition. SPE, SPE-124253-MS.
Wang, M., Wilkins, R.W., Song, G., Zhang, L., Xu, X., Li, Z., et al., 2015. Geochemical and geological characteristics of the Es3L lacustrine shale in the Bonan sag, Bohai Bay Basin, China. Inter. J. Coal Geol. 138, 16–29.
Wang, S., Feng, Q., Javadpour, F., Xia, T., Li, Z., 2015. Oil adsorption in shale nanopores and its effect on recoverable oil-in-place. Int. J. Coal Geol. 147, 9–24.
Wang, S., Javadpour, F., Feng, Q., 2016. Molecular dynamics simulations of oil transport through inorganic nanopores in shale. Fuel 171, 74–86.
Wang, M., Ma, R., Li, J., Lu, S., Li, C., Guo, Z., et al., 2019. Occurrence mechanism of lacustrine shale oil in the Paleogene Shahejie Formation of Jiyang depression, Bohai Bay Basin, China. Petrol. Explor. Dev+ 46 (4), 833–846.
Wang, Y., Liu, L., Hu, Q., Hao, L., Wang, X., Sheng, Y., 2020. Nanoscale pore network evolution of Xiamaling marine shale during organic matter maturation by hydrous pyrolysis. Energy Fuel. 34 (2), 1548–1563.
Wang, X., Wang, M., Li, J., Shao, H., Deng, Z., Wu, Y., 2022. Thermal maturity: the controlling factor of wettability, pore structure, and oil content in the lacustrine Qingshankou shale, Songliao Basin. J. Petrol. Sci. Eng. 215, 1–15, 110618.
Wood, D.A., Hazra, B., 2017. Characterization of organic-rich shales for petroleum exploration & exploitation: a review-part 1: bulk properties, multi-scale geometry and gas adsorption. J. Earth Sci. 28 (5), 739–757.
Wu, H., Hu, W., Cao, J., Wang, X., Wang, X., Liao, Z., 2016. A unique lacustrine mixed dolomitic-clastic sequence for tight oil reservoir within the middle Permian Lucaogou Formation of the Junggar Basin, NW China: Reservoir characteristics and origin. Mar. Petrol. Geol. 76, 115–132.
Wu, H., Hu, W., Wang, Y., Tao, K., Tang, Y., Cao, J., et al., 2021. Depositional conditions and accumulation models of tight oils in the middle Permian Lucaogou Formation in Junggar Basin, northwestern China: new insights from geochemical analysis. AAPG Bull. 105 (12), 2477–2518.
Xi, Z., Tang, S., Wang, J., Yang, G., Li, L., 2018a. Formation and development of pore structure in marine-continental transitional shale from northern China across a maturation gradient: insights from gas adsorption and mercury intrusion. Int. J. Coal Geol. 200, 87–102.
Xi, Z., Wang, J., Hu, J., Tang, S., Xiao, H., Zhang, Z., et al., 2018b. Experimental investigation of evolution of pore structure in Longmaxi marine shale using an anhydrous pyrolysis technique. Mineral 8 (6), 226.
Xu, Y., Lun, Z., Pan, Z., Wang, H., Zhou, X., Zhao, C., et al., 2022. Occurrence space and state of shale oil: a review. J. Petrol. Sci. Eng. 211, 1–14, 110183.
Yang, J., Hatcherian, J., Hackley, P.C., Pomerantz, A.E., 2017. Nanoscale geochemical and geomechanical characterization of organic matter in shale. Nat. Commun. 8 (1), 2179.
Yao, Y., Liu, D., 2012. Comparison of low-field NMR and mercury intrusion porosimetry in characterizing pore size distributions of coals. Fuel 95, 152–158.
Yong, W., Xuejun, W., Guoqi, S., Huimin, L., Deshun, Z., Deyan, Z., et al., 2016. Genetic connection between mud shale lithofacies and shale oil enrichment in Jiyang Depression, Bohai Bay Basin. Petrol. Explor. Dev+ 43 (5), 759–768.
Zhang, S., Liu, C., Liang, H., Wang, J., Bai, J., Yang, M., et al., 2018. Paleoenvironmental conditions, organic matter accumulation, and unconventional hydrocarbon potential for the Permian Lucaogou Formation organic-rich rocks in Santanghu Basin, NW China. Int. J. Coal Geol. 185, 44–60.
Zhao, J., Hu, Q., Liu, K., Jin, Z., Dultz, S., Kaufmann, J., et al., 2020. Pore connectivity characterization of shale using integrated wood's metal impregnation, microscopy, tomography, tracer mapping and porosimetry. Fuel 259, 1–10, 116248.
Zhen, Q., Zhensheng, S., Dazhong, D., Bin, L., Zhang, C., Jie, Z., et al., 2016. Geological characteristics of source rock and reservoir of tight oil and its accumulation mechanism: a case study of Permian Lucaogou Formation in Jimusar sag, Junggar Basin. Petrol. Explor. Dev+ 43 (6), 1013–1024.
Zhong, J., Wang, P., Zhang, Y., Yan, Y., Hu, S., Zhang, J., 2013. Adsorption mechanism of oil components on water-wet mineral surface: a molecular dynamics simulation study. Energy 59, 295–300.
Zou, C.N., Dong, D.Z., Wang, S.J., Li, J.Z., Li, X.J., Wang, Y.M., et al., 2010. Geological characteristics and resource potential of shale gas in China. Petrol. Explor. Dev+ 37 (6), 641–653.
Zou, C.N., Yang, Z., Cui, J.W., Zhu, R.K., Hou, L.H., Tao, S.Z., et al., 2013. Formation mechanism, geological characteristics and development strategy of nonmarine shale oil in China. Petrol. Explor. Dev+ 40 (1), 15–27.
Zou, C.N., Pan, S.Q., Jing, Z.H., Gao, J.L., Yang, Z., Wu, S.T., et al., 2020. Shale oil and gas revolution and its impact. Acta Petrol. Sin. 41 (1), 1.